Velocity Dependence of the Adiabatic Rapid Passage Force in Metastable Helium

A Dissertation Presented

by

Brian Arnold

to

The Graduate School

in Partial Fulfillment of the Requirements

for the Degree of

Doctor of Philosophy

in

Physics and Astronomy

Stony Brook University

December 2019

Stony Brook University

The Graduate School

Brian Arnold

We, the dissertation committee for the above candidate for the Doctor of Philosophy degree, hereby recommend acceptance of this dissertation.

Harold Metcalf – Dissertation Advisor
Distinguished Teaching Professor, Department of Physics and Astronomy

Matthew Dawber – Chairperson of Defense
Graduate Program Director, Department of Physics and Astronomy

Konstantin K. Likharev
Distinguished Toll Professor, Department of Physics and Astronomy

Sean J. Bentley
Associate Professor, Department of Physics
Adelphi University

This dissertation is accepted by the Graduate School.

Eric Wertheimer
Dean of the Graduate School

Abstract of the Dissertation

Velocity Dependence of the Adiabatic Rapid Passage Force in Metastable Helium

by

Brian Arnold

Doctor of Philosophy

in

Physics and Astronomy

Stony Brook University

2019

From optical tweezers to Doppler molasses and magneto-optical traps, optical forces have been a powerful tool for advancing control of quantum systems. Recent experiments have explored optical forces relying on stimulated emission rather than spontaneous emission. The Adiabatic Rapid Passage (ARP) force uses alternating chirped light pulses to excite and stimulate atoms providing a coherent momentum exchange. To determine the usefulness of the ARP force, we measure its velocity dependence. The velocity dependence contains large peak and valley structures we did not expect to see. To better explore the structures, we measure the force as a function of Rabi frequency and chirp range for a particular set of velocities. The evolution of the force remains unclear and requires

additional study, for which I have laid out a roadmap for future work.

For Melissa

Contents

List of Figures ix

Acknowledgements xii

1 Introduction 1

1.1 Two-Level Atom 2

1.2 Rotating Wave Approximation 5

1.3 Optical Bloch Equations 7

1.4 Light Shift 10

1.5 Dressed Atom 11

2 Optical Forces 14

2.1 Radiative Force 15

2.2 Dipole Force 17

2.3 Bichromatic Force 18

2.4 Other Polychromatic Forces 23

3 Theory of Adiabatic Rapid Passage 25

3.1 Adiabatic Rapid Passage 25

3.2 ARP Force Sequence 28
3.3 ARP Force Parameters 33
3.4 ARP on Moving Atoms 35

4 Metastable Helium Apparatus 39
4.1 Metastable Helium Source 39
4.2 Interaction Chamber 43
4.3 Detection Chamber 44

5 ARP Light Production 48
5.1 DL 100 Lasers 49
5.1.1 Laser Cavity 49
5.1.2 Master Laser Frequency Locking 50
5.1.3 Slave Laser Phase Locking 52
5.2 Electro-optic Modulators 55
5.2.1 Phase Modulator 55
5.2.2 Amplitude Modulator 58
5.2.3 Pulse Characterization 60
5.3 Amplifiers 62
5.3.1 Booster Optical Amplifiers 62
5.3.2 Fiber Amplifiers 63
5.4 Optical Transport 63
5.5 Alignment Procedure 64

6 Measurement of Optical Forces 67
6.1 Initial ARP Force Parameters 67

6.2 Force *vs.* Velocity 69
6.3 Force Parameter Search 74

7 Outlook 78
7.1 Interaction Time 78
7.2 Longitudinal Slowing 79
7.3 Conventional ARP 80

Bibliography 81

List of Figures

1.1 Two-Level Atom 3
1.2 Rabi Oscillations 6
1.3 Bloch Sphere 8
1.4 Light Shift 11
1.5 Dressed State 12

2.1 Radiative Force 16
2.2 Bichromatic Two Level Atom 18
2.3 Doubly Dressed Atom 19
2.4 Bichromatic Eigenenergies 21
2.5 Bichromatic Force Profile 22
2.6 Bichromatic Velocity Dependence 23

3.1 ARP Dressed States 26
3.2 Generalized ARP Force Sequence 29
3.3 ARP Pulse Timing Schemes 29
3.4 Force *vs.* Dead Time 31
3.5 ARP Force Sequence 32
3.6 Numerical Simulation Forcemaps 34

3.7 ARP Bloch Sphere 35
3.8 Doppler Shifted Chirp 36
3.9 Numerical Velocity Dependence 37

4.1 Vacuum System 40
4.2 Energy Level Diagram for Helium 41
4.3 Optical Pumping 42
4.4 Helium Source 43
4.5 Atomic Slit and Helmholtz Coils 44
4.6 MCP/PS Diagram 45
4.7 Phosphor Screen Image 47

5.1 Complete Laser System 48
5.2 DL 100 50
5.3 SAS Diagram and Digilock 51
5.4 Phase Lock 53
5.5 Phase and Amplitude Modulators 56
5.6 Fabry-Perot Interferometer 59
5.7 Optical Pulses 60
5.8 FP Pulse Spectrum 61
5.9 FP Pulse and Chirp Spectrum 61

6.1 Experimental Forcemap 68
6.2 Force vs. Velocity for Regions 1 and 2 70
6.3 Force vs. Velocity for Region 1, Averaged 72
6.4 Force vs. Velocity for 300 and 200 Pulse Pairs 73

6.5 Forcemap Parameter Range 74
6.6 Forcemap Array 75

Acknowledgements

As I come to the end of this process, I find myself thinking about all the people who helped and supported me along the way. There are so many, I don't think I could name them all. But there are some people who I am especially thankful for that I will mention here. Words are not my strength. I wish I could give each of you the biggest, warmest hug. I hope this will suffice instead.

First, I am most grateful to God. He guides and sustains me, especially in the Sacraments. I thank Him for providing me with the capability to perform the work required, for surrounding me with people to support me, and for offering so many opportunities to push myself and grow.

I want to thank my wife, Melissa, who has stood by me through the turmoil of Ph.D. life. She has been my biggest supporter, my confidant, my best friend. I couldn't have done this without you, darling. I can't wait to see how we will blossom as we begin the next chapter of our lives.

My parents, Linda and Tony, in-laws, Sandi and Glenn, and brother, Kevin, have been invaluable to me. Their love and support have carried me through the difficult times in the program and always given a place of respite, away from the stress. Thank you for believing in me.

None of this would have ever happened if not for my advisor, Dr. Harold Metcalf, who

took a shot on me in the summer of 2011. Hal has always made it clear that he cares deeply for the personal lives of myself and the other members of the lab, not just for what we can accomplish in the lab. I will miss our spirited debates and lively discussions.

The members of the Metcalf group, past and present, have been a great source of support over the years. Chris Corder, Dan Stack, Yuan Sun, and John Elgin graciously welcomed me into the lab and helped me to find my footing. I am grateful to them for their patience and all they taught me when I was new to the lab. Petr Anisimov and Mary Lyon were incredible mentors and resources during my time here. Taichi Inaki, He Zhang, and Deqian Yuan joined along the way and have since also left to begin their careers. It was great rubbing elbows with you all; thank you for keeping me sane.

I am also thankful to my fellow graduate students, post-docs and undergraduates from the Metcalf group and Laser Teaching Center who have assisted me since I became the senior student of the lab: Yifan Fang, Xiaoyang Liu, Ian Schwartz, and Eli Rafkin, you have my thanks and best wishes as you continue the work we've done And to Thomas Mittiga, James Dragan, Xiang Hua, Seth Berl, Casey McKenna, Max Stanley, Stefan Evans, Jessica Gasparik, Anthony Orlando, David Siegel, and Willa Dworschack, thank you for literally lending a hand when I needed it. I hope that I have been able to pass on everything that was taught to me, and that I can continue to be helpful for you as you move forward.

Graduate school is notoriously difficult for everyone, but my friends in the Department of Physics and Astronomy that have taken this journey with me have bolstered my spirits in an incredible way. From lunches to Friday socials, weekend barbecues or late-night talks, the camaraderie in the basement really helped get me through. Spencer Horton, Ludwig Krinner, Hans Niederhausen, Bertus Jordaan, Peter Sandor, Arthur Zhao, Oumarou Njoya, Arturo Pazmino, Medhi Namazi, Abhishodh Prakash, Ben Bein, Raghav Kunnawalkam, Mael Flament, Samet Demircan, Yusong Liu, Brian Kaufman, Myles Silfies, Mike Stewart,

Joonhyuk Kwon, Chuan Cheng, Guodong Cui, and Sonali Gera, I am honored to call you my friends and colleagues.

The department couldn't work without its incredible staff. Over the years I have benefited from the kindness and care of the main office staff, Sara Lutterbie, Donnie Sheehan, Linda Dixon, Socorro Delquaglio, Jin Bentley, Vicki Grove, Nathan Leoce-Schappin, Axel Drees, Laszlo Mihaly, Matt Dawber, and Jac Verbaarschot. My experiment would never have gotten off the ground without the building and technical staff, Bob Segnini, Frank Chin, Rich Berscak, Rich Lefferts, Gene Shafto, Chuck Pancake, Paul DiMatteo, James Eksi, Mark Jablonski, Jeffrey Slechta, and Jeffrey Thomas (JT).

Stony Brook has allowed me to make wonderful friends from all backgrounds and walks of life, and they are what I treasure most about my time on Long Island. Most of all, I am grateful to my Newman family, Stony Brook's Catholic Campus Ministry. You all have loved me at my best and my worst and have surrounded me with prayers, advice and support for years. It means more than I can say. I thank God for the gift of Joanne Buonocore, Marianne Sheridan, Fr. Bob Smith, Fr. Sean Magaldi, Fr. Lachlan Cameron, Mike & Maribel Saccomanno, Dominik Wegiel, Gilmary George, Emily Acosta, Marty Smyth, Nick Salerno, Ryan McKenna, Benedette Adewale, Theresa Marino, Alicia Chionchio, Marie Cushmore, Tommy Imbornoni, Stephanie Catarino, Gloria Lee, Nick Chapman, Jeena Rudy, Megan Vantslot, Monique Brutus and family, Susan Morgenlander, Doug Orenstein, Mariya George, Phil Mauser, Kaitlyn Colgan, Ryan "Sebastian" Edmundson, Visal Poornaka, Sam Parker, Fr. Cody Bobick, Ryan Gallagher, and Stephen Sham.

And last but not least, my friends outside of SBU have each found ways of pulling me out of the stress and helping me to see the light at the end of this long tunnel. Liz & Dave Teixeira, Mikey Colosa, Lauren Haile, Meg & George Warner, John Nichols, Frank Martini, Norrel Sainsott, Nick & Ashley Kowalski, and Mike Chiappone, thank you for always being

there for me.

Chapter 1

Introduction

Laser cooling and trapping has been a tremendous resource to the atomic physics community [1–6]. Developments over the past four decades have led to great improvements in the precision control of atoms and ions [7–13]. As the field continues to grow, the focus of some new techniques has shifted to the direct laser cooling and trapping of molecules [14–21].

Molecular systems can differ from atomic systems in many ways, but the key differences in terms of laser cooling and trapping are the typically larger masses and the general lack of cycling transitions [22].

Cooling or trapping a particle with a larger mass requires a larger force, a longer interaction time, or some combination of these. Zeeman slowers are effective at broadening the velocity dependence and therefore increase the interaction time but at the cost of a larger footprint [23]. Larger optical forces would reduce the need for this or even help in achieving greater minimization of existing experiments.

Single frequency optical forces rely upon spontaneous emission to remove energy and entropy from the atomic system [24]. To expand these techniques to a system without a cycling transition, would require a large number of re-pump lasers. Polychromatic optical

forces offer the ability to use stimulated emission to remove energy from the system as well as return the atom or molecule to its original state so it can be acted upon again [25].

There has been some debate as to whether or not polychromatic optical forces can remove entropy from the system [26]. It is not inherent to all polychromatic optical forces, but rather each must be considered individually. The bichromatic optical force (see Sec. 2.3) has been shown theoretically [25, 26], experimentally [27, 28], and in simulations [28, 29] to be able to remove entropy from the system without the need for spontaneous emission. We have not yet rigorously considered this question for the ARP force.

In this chapter, we lay down the underlying concepts and mathematics necessary for discussing optical forces. Chap. 2 puts these concepts to use in an overview of other popular optical forces that have emerged. Chap. 3 covers the theory of ARP and its use as a force. Chap. 4 and 5 describe the vacuum system and light production used in our experiments. Chap. 6 discusses the results of our experiments. Chap. 7 lays out possible pathways for future experiments.

1.1 Two-Level Atom

Two-level systems have been extensively studied for use in numerous areas of physics. Using this framework to describe two states within an atom or molecule creates a convenient playground for exploring interactions between light and matter. The two-level atom approximation precludes concern about light polarization selection rules, dipole moment orientation, or other such things because it is conceptually equivalent to a spin-one-half particle in a magnetic field [3]. Our discussion of this will primarily follow that of Ref. [2, 30, 31]

We will explore this model, beginning with the time-dependent Schrödinger equation

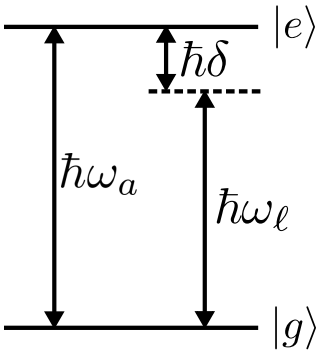

Figure 1.1: Energy level diagram for a two-level atom. $\hbar\omega_a$ is the energy difference between the ground state $|g\rangle$ and the excited state $|e\rangle$. The laser frequency is ω_ℓ and can be detuned by $\delta \equiv \omega_\ell - \omega_a$ from atomic resonance.

(TDSE)

$$\mathcal{H}\Psi(\mathbf{r},t) = i\hbar\frac{\partial}{\partial t}(\Psi(\mathbf{r},t)), \tag{1.1}$$

where the Hamiltonian is of the form

$$\mathcal{H} = \mathcal{H}_0 + \mathcal{H}'(t), \tag{1.2a}$$

$$\mathcal{H}_0 = \hbar\omega_g|g\rangle\langle g| + \hbar\omega_e|e\rangle\langle e|, \tag{1.2b}$$

$$\mathcal{H}'(t) = -\overrightarrow{d}(t)\cdot\overrightarrow{E}(t) = \hbar\Omega_R(t)|g\rangle\langle e| + \hbar\Omega_R^*(t)|e\rangle\langle g|, \tag{1.2c}$$

where $\mathcal{H}_0$ is the bare atomic Hamiltonian, $\mathcal{H}'(t)$ describes the interaction of the light field with the dipole moment, and

$$\Omega_R(t) = -\frac{\overrightarrow{d}(t)\cdot\overrightarrow{E}(t)}{\hbar}. \tag{1.3}$$

We can make an insightful choice of a basis state for our system:

$$|\psi\rangle = c_g(t)\mathrm{e}^{-i\omega_g t}|g\rangle + c_e(t)\mathrm{e}^{-i\omega_e t}|e\rangle \tag{1.4}$$

and plug this into Eqn. 1.1

$$i\hbar\frac{d}{dt}|\psi\rangle = \mathcal{H}(t)|\psi\rangle. \tag{1.5}$$

After some algebra, this leads to the set of coupled differential equations:

$$\dot{c}_g(t) = -i\Omega_R(t)\mathrm{e}^{-i\omega_a t}c_e(t), \tag{1.6a}$$

$$\dot{c}_e(t) = -i\Omega_R^*(t)\mathrm{e}^{-i\omega_a t}c_g(t), \tag{1.6b}$$

where $\omega_a \equiv \omega_e - \omega_g$ is the atomic resonance frequency.

We can write down the electric field of the laser as

$$\overrightarrow{E}(t) = \mathcal{E}\hat{\epsilon}\cos(\omega_\ell t) \tag{1.7}$$

where $\mathcal{E}$ contains the spatial dependence of the field, $\hat{\epsilon}$ is the polarization vector, and ω_ℓ is the frequency of the laser. We can plug this into Eqn. 1.3 giving us

$$\Omega_R(t) = -\left(\frac{\mathcal{E}}{\hbar}\overrightarrow{d}(t)\cdot\hat{\epsilon}\right)\cos(\omega_\ell t) = \Omega\cos(\omega_\ell t). \tag{1.8}$$

We can use this in Eqn. 1.6 to give us

$$\dot{c}_g(t) = -i\frac{\Omega}{2}(\mathrm{e}^{-i(\omega_\ell+\omega_a)t} + \mathrm{e}^{i(\omega_\ell-\omega_a)t})c_e(t), \tag{1.9a}$$

$$\dot{c}_e(t) = -i\frac{\Omega^*}{2}(\mathrm{e}^{-i(\omega_\ell-\omega_a)t} + \mathrm{e}^{i(\omega_\ell+\omega_a)t})c_g(t). \tag{1.9b}$$

1.2 Rotating Wave Approximation

We can now see two relevant frequencies emerge, fast: $\omega_\ell + \omega_a$ and slow: $\omega_\ell - \omega_a$. The fast oscillations occur too quickly for normal experiments ($\sim 10^{15}$Hz). The rotating wave approximation (RWA) assumes that these oscillations average to zero and can safely be ignored [32]. This allows us to consider only the slow frequency $\delta \equiv \omega_\ell - \omega_a$ (up to a few hundred MHz) giving us

$$\dot{c}_g(t) = -i\frac{\Omega}{2}\mathrm{e}^{i\delta t}c_e(t), \tag{1.10a}$$

$$\dot{c}_e(t) = -i\frac{\Omega^*}{2}\mathrm{e}^{-i\delta t}c_g(t). \tag{1.10b}$$

In order to decouple the two equations, we can take the second derivative and substitute each one back into the opposite equation giving us

$$\ddot{c}_g(t) - i\delta\dot{c}_g(t) + \frac{|\Omega|^2}{4}c_g(t) = 0, \tag{1.11a}$$

$$\ddot{c}_e(t) + i\delta\dot{c}_e(t) + \frac{|\Omega|^2}{4}c_e(t) = 0. \tag{1.11b}$$

With the initial conditions $c_g(0) = 1$ and $c_e(0) = 0$, we can directly solve these equations to give

$$c_g(t) = \left(\cos\frac{\Omega' t}{2} - i\frac{\delta}{\Omega'}\sin\frac{\Omega' t}{2}\right)\mathrm{e}^{i\delta t/2}, \tag{1.12a}$$

$$c_e(t) = \left(-i\frac{\Omega_0 e^{i\phi}}{\Omega'}\sin\frac{\Omega' t}{2}\right)\mathrm{e}^{i\delta t/2} \tag{1.12b}$$

where $\Omega' \equiv \sqrt{|\Omega|^2 + \delta^2}$ is the generalized Rabi frequency. Now we can square these to find the observable state populations:

$$|c_g(t)|^2 = 1 - \left(\frac{\Omega}{\Omega'}\right)^2 \sin^2\frac{\Omega' t}{2}, \tag{1.13a}$$

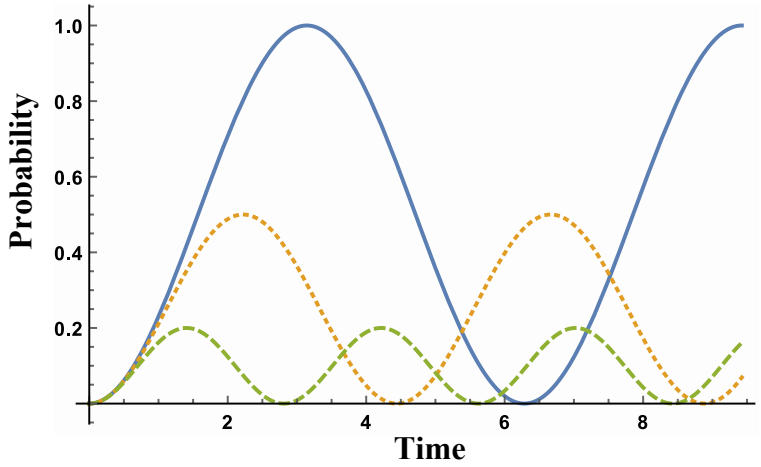

Figure 1.2: Plot of the probability of an atom to be found in the excited state, $|c_e(t)|^2$, vs. time. The solid line corresponds to $\delta = 0$, the dotted line to $\delta = |\Omega|$, and the dashed line to $\delta = 2|\Omega|$. The time is plotted in units of $1/|\Omega|$.

$$|c_e(t)|^2 = \left(\frac{\Omega}{\Omega'}\right)^2 \sin^2 \frac{\Omega' t}{2}. \tag{1.13b}$$

The oscillations of $|c_e(t)|^2$ (shown in Fig. 1.2) are known as Rabi oscillations or Rabi flopping. For $\delta = 0$, the wavefunction will oscillate between the two states, but for $\delta \neq 0$, $|c_e(t)|^2$ never reaches a probability of 1.

We can also use Fig. 1.2 to see that for a resonant light field ($\delta = 0$), a pulse of duration $t = \pi/\Omega$ results in complete inversion, $|c_e(t)|^2 = 1$, and is known as a π-pulse. Similarly, a pulse of duration $t = \pi/(2\Omega)$ places the atom in an equal superposition of ground and excited states, $|c_g(t)|^2 = |c_e(t)|^2 = 0.5$, and is known as a $\pi/2$-pulse.

At this point, our derivations will diverge along two parallel paths. This will allow us to investigate different facets of the system.

1.3 Optical Bloch Equations

First, the time-dependence of this system can be further explored using the density matrix formalism [33]. This allows us to view the partial state coherences in conjunction with the observable state populations. We can write the density matrix as

$$\rho \equiv \begin{pmatrix} \rho_{gg} & \rho_{ge} \\ \rho_{eg} & \rho_{ee} \end{pmatrix} = |\psi\rangle\langle\psi| = \begin{pmatrix} |c_g|^2 & c_g c_e^* \\ c_e c_g^* & |c_e|^2 \end{pmatrix}. \tag{1.14}$$

From this density matrix, we can choose a change of variables to a rotating coordinate system [34]. We can create an artificial state vector, called the Bloch vector:

$$\overrightarrow{R} = (u, v, w), \tag{1.15}$$

where

$$|\overrightarrow{R}(t)| = |c_g|^2 + |c_e|^2 = 1. \tag{1.16}$$

Its unit length confines it to a unit sphere or Bloch sphere. The south pole of this sphere represents the ground state and the north pole represents the excited state. All other locations on the sphere represent a superposition of ground and excited states.

Because the combination of identity matrix I and the Pauli matrices span the two dimensional Hilbert space, we can use them in order to rewrite the Bloch vector into components:

$$\langle\sigma_x\rangle = \begin{pmatrix} c_e^* & c_g^* \end{pmatrix} \begin{pmatrix} 0 & 1 \\ 1 & 0 \end{pmatrix} \begin{pmatrix} c_e \\ c_g \end{pmatrix} = c_g c_e^* + c_g^* c_e = u, \tag{1.17a}$$

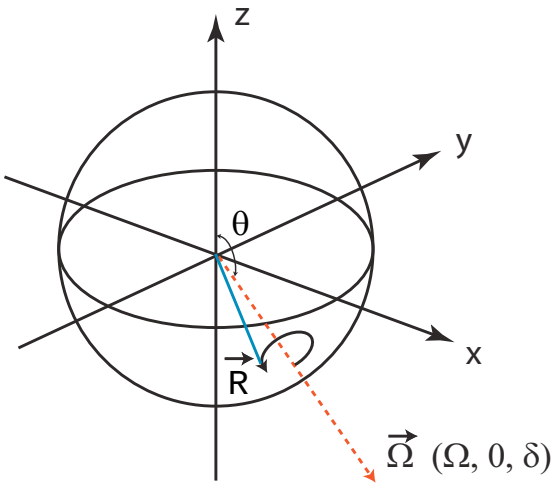

Figure 1.3: The projection of the Bloch vector, $\overrightarrow{R}$, and torque vector, $\overrightarrow{\Omega}$, onto the Bloch sphere. $\overrightarrow{R}$ can be seen precessing about $\overrightarrow{\Omega}$.

$$\langle \sigma_y \rangle = \begin{pmatrix} c_e^* & c_g^* \end{pmatrix} \begin{pmatrix} 0 & i \\ -1 & 0 \end{pmatrix} \begin{pmatrix} c_e \\ c_g \end{pmatrix} = i(c_g c_e^* - c_g^* c_e) = v, \tag{1.17b}$$

$$\langle \sigma_z \rangle = \begin{pmatrix} c_e^* & c_g^* \end{pmatrix} \begin{pmatrix} 1 & 0 \\ 0 & -1 \end{pmatrix} \begin{pmatrix} c_e \\ c_g \end{pmatrix} = |c_e|^2 - |c_g|^2 = w. \tag{1.17c}$$

By reworking Eqn. 1.10 in terms of the Bloch vector, we can write the time dependence of the Bloch vector as

$$\frac{d\overrightarrow{R}}{dt} = \overrightarrow{\Omega} \times \overrightarrow{R} \tag{1.18}$$

where $\overrightarrow{\Omega} = (\Omega_{Real}, \Omega_{Imag}, -\delta)$ is known as the torque vector, giving us

$$\dot{u} = \Omega_{Imag} w - \delta v, \tag{1.19a}$$

$$\dot{v} = -\Omega_{Real} w + \delta u, \tag{1.19b}$$

$$\dot{w} = \Omega_{Real} v - \Omega_{Imag} u. \tag{1.19c}$$

To better describe a real atomic system, we must also consider possible relaxation effects that can decohere the system. Typically, these decoherence effects fall into one of two timescales [6]. $\gamma = 1/\tau$ is the spontaneous decay rate, the inverse of the excited state lifetime. It describes how fast the population relaxes to equilibrium, in this case, to the ground state. Γ is the pure dephasing rate, primarily from interactions with the environment such as collisions. In most systems, these can be combined into a single coherence decay rate:

$$\gamma_{12} = \frac{\gamma}{2} + \Gamma. \tag{1.20}$$

From this, we can rederive [6] the time dependence of $\overrightarrow{R}$ to be

$$\dot{u} = \Omega_{Imag} w - \delta v - \gamma_{12} u, \tag{1.21a}$$

$$\dot{v} = -\Omega_{Real} w + \delta u - \gamma_{12} v, \tag{1.21b}$$

$$\dot{w} = \Omega_{Real} v - \Omega_{Imag} u - \gamma(w + 1). \tag{1.21c}$$

In our particular experiment, atoms in the beam are a very dilute sample at the interaction region and therefore collisions can be ignored. In this limit, Γ is negligible and therefore $\gamma_{12} \to \gamma/2$. This allows us to simplify Eqn. 1.21 to

$$\dot{u} = \Omega_{Imag} w - \delta v - (\gamma/2) u, \tag{1.22a}$$

$$\dot{v} = -\Omega_{Real} w + \delta u - (\gamma/2) v, \tag{1.22b}$$

$$\dot{w} = \Omega_{Real} v - \Omega_{Imag} u - \gamma(w + 1). \tag{1.22c}$$

Eqn. 1.22 are commonly referred to as the optical Bloch equations (OBE's).

1.4 Light Shift

Now we can return to the oscillating nature of Eqn. 1.13 shown in Fig. 1.2. This oscillating solution suggests that the bare atomic states are no longer the eigenstates of the system. We can find the eigenstates by performing a coordinate transformation to a frame rotating at a rate of δ:

$$c'_g(t) = c_g(t)\mathrm{e}^{-i\delta t/2}, \tag{1.23a}$$

$$c'_e(t) = c_e(t)\mathrm{e}^{i\delta t/2}. \tag{1.23b}$$

As before, we would plug this into Eqn. 1.1 leading us to a set of differential equations analogous to Eqn. 1.6:

$$\begin{pmatrix} \dot{c}'_g(t) \\ \dot{c}'_e(t) \end{pmatrix} = -\frac{i}{2}\begin{pmatrix} \delta & \Omega \\ \Omega^* & -\delta \end{pmatrix}\begin{pmatrix} c'_g(t) \\ c'_e(t) \end{pmatrix}. \tag{1.24}$$

By diagonalizing this matrix, we can solve for the eigenenergies and eigenstates [35] as

$$E_\pm = \pm\frac{\hbar}{2}\sqrt{|\Omega|^2 + \delta^2} = \pm\frac{\hbar\Omega'}{2}, \tag{1.25a}$$

$$|-\rangle = \sqrt{1/2(1+\delta/\Omega')}|\tilde{g}\rangle - \sqrt{1-1/2(1+\delta/\Omega')}|\tilde{e}\rangle, \tag{1.25b}$$

$$|+\rangle = \sqrt{1/2(1-\delta/\Omega')}|\tilde{g}\rangle + \sqrt{1-1/2(1-\delta/\Omega')}|\tilde{e}\rangle. \tag{1.25c}$$

Where $|\tilde{g}\rangle$ and $|\tilde{e}\rangle$ are the atomic states containing the time dependence of the rotating frame. The phase associated with this rotating frame will have no effect on the population evolution of the new eigenstates.

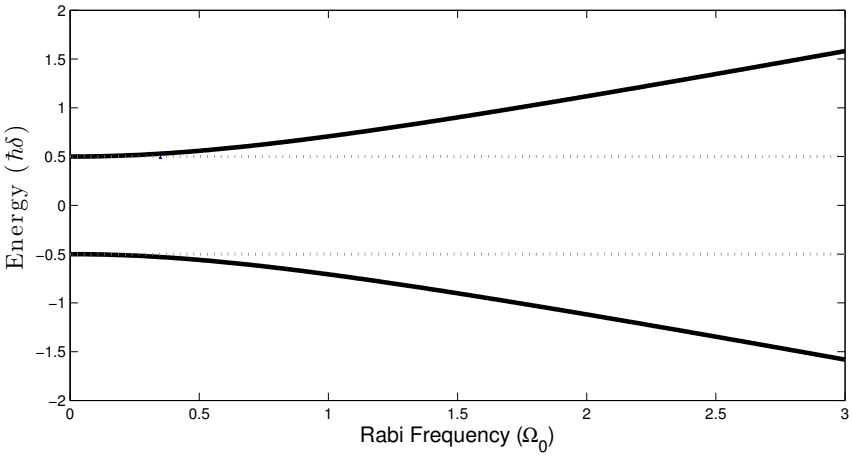

Figure 1.4: The eigenenergies are shifted proportionally to the Rabi frequency, Ω (written as Ω_0 because the image is borrowed from Ref. [31]).

By examining Eqn. 1.25a, we can see that for low intensities ($\Omega \sim 0$), the eigenstates are separated by $\hbar\delta$ and correspond to the dressed states (which we will discuss further in Sec. 1.5). As Ω increases, the eigenenergies separate and the eigenstates become a mixture of the atomic states. This separation can also be seen in Fig. 1.4.

1.5 Dressed Atom

We can also introduce a technique for understanding for the atom-light system together, rather than as two separate entities. We will adapt the previous Hamiltonian of Eqn. 1.2a into

$$\mathcal{H} = \mathcal{H}_0 + \mathcal{H}'(t) + \mathcal{H}_f(t) \tag{1.26}$$

where $\mathcal{H}_f(t)$ is the electric field Hamiltonian.

We can dress the system by combining both atomic state and optical field into one $|i, N\rangle$ where i can either be g or e and N denotes the number of excitations of the optical field.

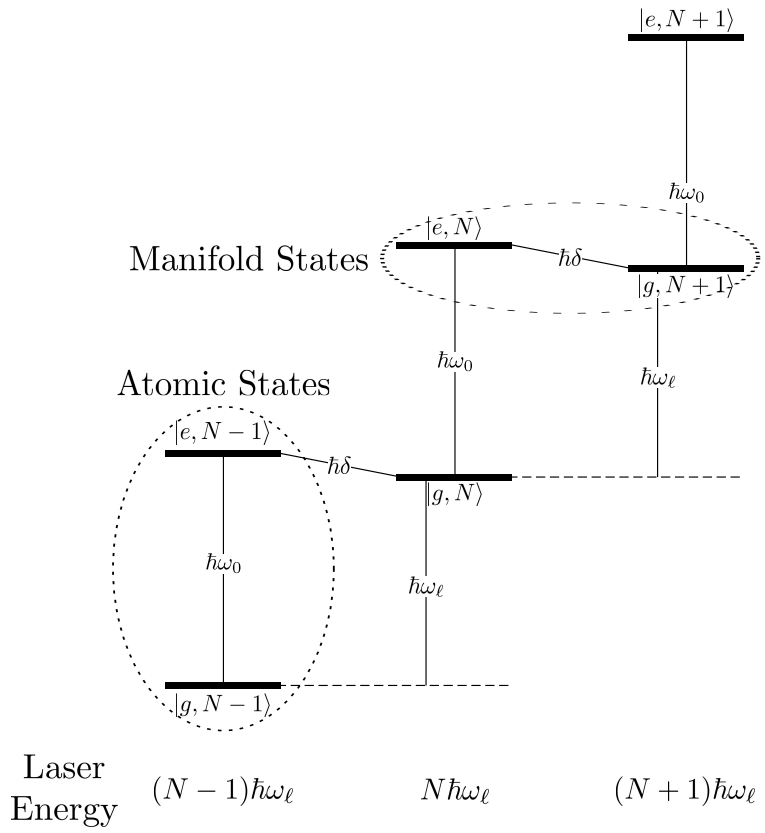

Figure 1.5: Level spectrum of the dressed states demonstrating both atomic and manifold states. This image is not to scale, as the separation of manifold states, $\hbar\delta$ is much smaller than the original atomic state energy, $\hbar\omega_a$ (written as $\hbar\omega_0$ because the image is borrowed from Ref. [31]).

The states $|g, N\rangle$ and $|e, N\rangle$ are separated by $\hbar\omega_a$ and the states $|g, N\rangle$ and $|g, N+1\rangle$ are separated by $\hbar\omega_\ell$, as seen in Fig. 1.5.

So far, this tells the story of the atomic states and the electric field separately. To get to the interesting dynamics of the dressed system, we can examine that the states $|g, N\rangle$ and $|e, N-1\rangle$ (referred to as manifold states) are separated by $\hbar\delta$. By moving from ground to excited state and the loss of one quanta of the electric field, the total energy change is nearly canceled out. This sets two scales for understanding the system: the large scale energy changes of only changing photon number or only changing atomic state, and the small scale

energy changes of changing manifold states.

Since each set of manifold states has an identical structure, we can consider our Hamiltonian (Eqn. 1.26) for an individual set of manifold states. This allows us to reduce the Hamiltonian to

$$\mathcal{H} = \frac{\hbar}{2}\begin{pmatrix} 0 & \Omega \\ \Omega^* & 2\delta \end{pmatrix}. \tag{1.27}$$

We can diagonalize this to find our new eigenenergies and eigenstates [36] to be

$$E_n = \frac{\hbar}{2}\left(\delta \pm \sqrt{|\Omega|^2 + \delta^2}\right) + \hbar\omega_\ell\left(n + \frac{1}{2}\right), \tag{1.28a}$$

$$|1\rangle = \sin\theta|g, N\rangle + \cos\theta|e, N-1\rangle, \tag{1.28b}$$

$$|2\rangle = \cos\theta|g, N\rangle - \sin\theta|e, N-1\rangle, \tag{1.28c}$$

where θ is a mixing angle defined by $\tan 2\theta = -\Omega/\delta$ for $0 \leq \theta < \pi/2$. By examining the eigenenergies, we can see that the separation grows as the Rabi frequency increases. This is the effect of the light shift we saw in Sec 1.4. The mixing of the atomic states also increases as the Rabi frequency increases. This is the effect of the Rabi oscillations we saw at the end of Sec 1.2.

We can also discuss relaxation of the system. Despite the energy separation of states $|1\rangle$ and $|2\rangle$, there is no direct relaxation between the states. Spontaneous emission will cause an emission of light into an arbitrary direction and therefore the emitted light will no longer be counted among the excitations of the light field we are considering. This causes the system to relax to a lower pair of manifold states rather than relaxation occuring within a given manifold state.

Chapter 2

Optical Forces

The basic principles of all optical forces are remarkably simple. Light carries easily quantifiable amounts of energy, momentum, and angular momentum. Every time an atom or molecule absorbs or emits light, we rely on the energy, momentum, and angular momentum conservation laws to account for changes in the system [1, 2, 5].

The energy absorbed, $\hbar\omega_\ell$, needs to match the change in internal energy of the atom, $\hbar\omega_a$. The angular momentum of the light, $\hbar$, matches the change in orbital angular momentum of the electron. Finally, the linear momentum of the light, $\hbar\omega_\ell/c \equiv \hbar k$, directly transfers to the atom's momentum. The resulting velocity change $v_r = \hbar k/M$ (where M is the mass of the atom) is typically a few cm/s.

The total strength of the force depends on the repetition rate of this process, typically limited by the rate of the atom's return to its ground state. In this section, we will explore how this principle is applied in a variety of schemes to produce optical forces.

2.1 Radiative Force

The radiative force is the simplest of the optical forces. As shown in Fig. 2.1, a stationary atom in a resonant laser field will absorb light and move from ground to excited state. The momentum of the absorbed light, $\hbar k$, will also transfer to the atom resulting in a momentum change in the same direction the laser beam is traveling. After some time (usually $\sim \tau$), the atom will undergo the process of spontaneous emission, which returns the atom to its ground state and emits light in a random direction. Since the light is carrying away $\hbar k$ of momentum, the atom will recoil in the opposite direction. Sometimes, this second momentum kick will be in a similar direction to the initial momentum kick, other times it will be almost perfectly opposed, and yet other times, it could be almost orthogonal. Over many cycles, these secondary recoils will average out to zero, but the momentum changes for absorption are all additive, giving a net momentum change in the direction the light is traveling.

As stated previously, the total strength of the force depends on the repetition rate of this process. In this case, it is limited by the spontaneous emission rate, γ, which allows the atom to return to its ground state. The force can simply be described by the momentum change per cycle multiplied by the repetition rate. Intuitively,

$$\overrightarrow{F}_{Rad} = \hbar \overrightarrow{k} \gamma, \tag{2.1}$$

but the repetition rate is not just the spontaneous emission rate, because the atom is not always in the excited state and therefore is not always able to emit light. The repetition rate requires the time averaged excited state population, $\overline{|c_e(t)|}^2$, giving us

$$\overrightarrow{F}_{Rad} = \hbar \overrightarrow{k} \gamma \overline{|c_e(t)|}^2 = \frac{\hbar \overrightarrow{k} \gamma}{2} \left(\frac{s_0}{1 + s_0 + (2\delta/\gamma)^2} \right) \tag{2.2}$$

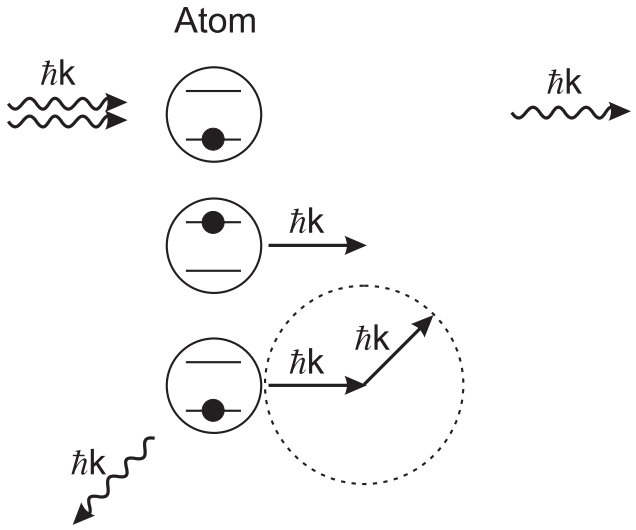

Figure 2.1: Diagram for a single cycle of the radiative force. An atom in the ground state absorbs light. The atom is excited and receives an $\hbar k$ momentum kick in the direction the light is traveling. Eventually the atom will undergo spontaneous emission and return to the ground state. This newly emitted light will travel in a random direction and the atom will recoil in the opposite direction. Over many cycles of this, the randomly directed recoils will average to zero and the atom is left with a net momentum change in the direction the light is traveling.

where s_0 is the saturation parameter and is defined [2] in terms of the laser intensity (I) and saturation intensity ($I_s = \frac{\pi hc}{3\lambda^3\tau}$) as

$$s_0 = \frac{I}{I_s} = 2\left(\frac{\Omega}{\gamma}\right)^2. \tag{2.3}$$

Under closer inspection, we can see that time averaged excited state population has a maximum value of 1/2 corresponding to $\delta = 0$ and $s_0 \gg 1$. This means the maximum force is

$$\overrightarrow{F}_{Rad,max} = \frac{\hbar \overrightarrow{k} \gamma}{2}. \tag{2.4}$$

To generalize this force for moving atoms, we must consider the Doppler shift given by $\omega_D = -\overrightarrow{k} \cdot \overrightarrow{v}$. This will naturally lead to an effective detuning, $\delta' = \delta + \omega_D$, allowing us to

rewrite Eqn. 2.2 as

$$\overrightarrow{F}_{Rad} = \frac{\hbar \overrightarrow{k} \gamma}{2} \left(\frac{s_0}{1 + s_0 + (2(\delta - \overrightarrow{k} \cdot \overrightarrow{v})/\gamma)^2} \right). \tag{2.5}$$

With this change, the magnitude of the maximum force remains the same, but now occurs when $\delta' = 0$. This tells us that atoms with a velocity $\overrightarrow{v} = \delta \overrightarrow{k}/k^2$ will experience the maximum force.

2.2 Dipole Force

A second optical force we can discuss is the optical dipole force. This force relies on the light shift [2, 37] we explored in Sec. 1.4. For an atom in a standing wave, the spatial dependence of the light field and Rabi frequency can be described by

$$I(z) = I_0 \cos^2(kz), \tag{2.6a}$$

$$\Omega(z) = \Omega_{max} \cos(kz). \tag{2.6b}$$

As we saw in Eqn. 1.25a, the energies of the eigenstates are dependent on the Rabi frequency and will, therefore, also follow this spatial dependence. From the Ehrenfest theorem [2], the gradient of the potential energy surface gives the dipole force

$$\overrightarrow{F}_{dip} = -\nabla \mathcal{H} = -\nabla \frac{\hbar}{2} \sqrt{|\Omega(z)|^2 + \delta^2}. \tag{2.7}$$

It is important to note that the radiative force and dipole force can occur at the same time, which is why it is often primarily only considered for large detunings, $\delta \gg \Omega$,

$$\overrightarrow{F}_{dip} = -\nabla \frac{\hbar|\Omega(z)|^2}{4\delta} = \frac{\hbar k \gamma^2 I_0}{8\delta I_{sat}} \sin(2kz). \tag{2.8}$$

The first thing to note about this force is that it does not saturate with intensity like the radiative force. Instead, it grows proportionately with intensity. The directionality of the force varies spatially at twice the spatial frequency of the standing wave. This leads to an average force of 0 across $^1/_2$ of a wavelength.

2.3 Bichromatic Force

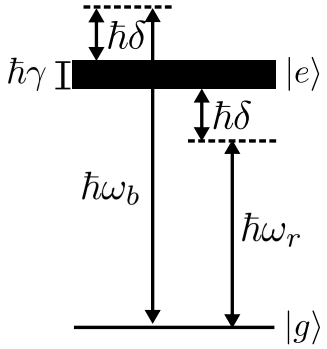

Figure 2.2: Energy level diagram for a two level atom. The bichromatic force uses two frequencies, $\omega_{r,b}$, detuned equally above and below resonance by $\delta \gg \gamma$. The width of the excited state line is exaggerated to display the linewidth of the transition.

To open the discussion of polychromatic forces, we can begin with the bichromatic force. As the name implies, the bichromatic force makes use of two optical frequencies, $\omega_{r,b}$, detuned equally above and below resonance by $\delta \gg \gamma$, as seen in Fig. 2.2. Both light fields are arranged as standing waves.

The bichromatic force is often described by two very different methods: the π pulse

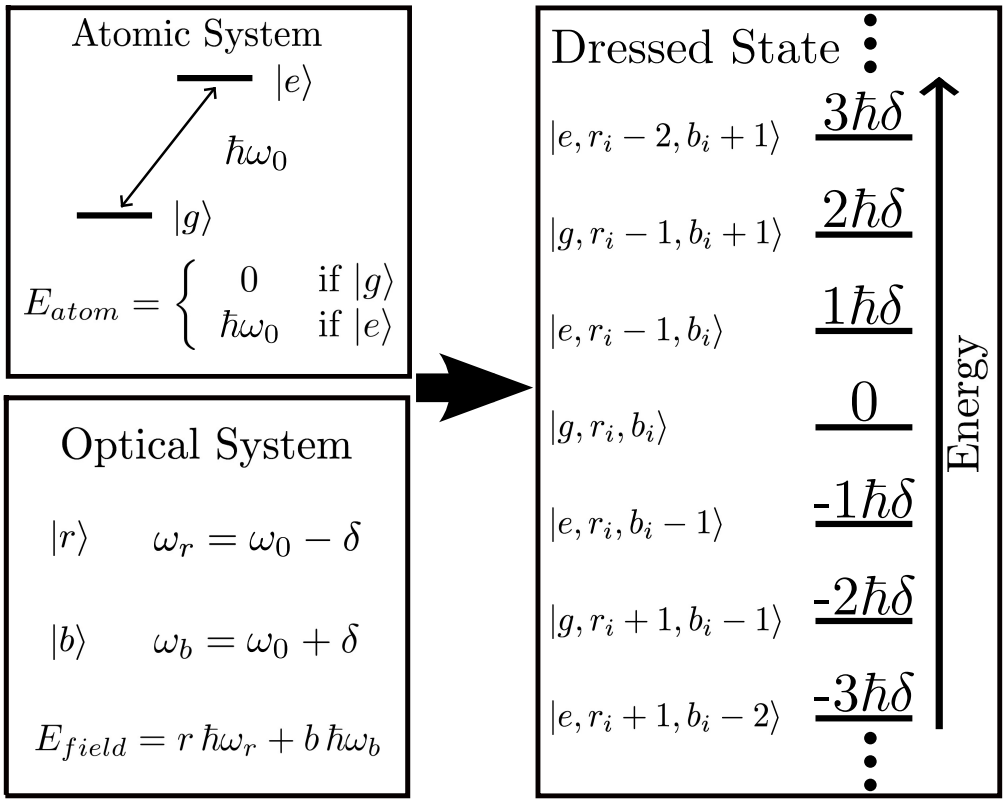

Figure 2.3: This figure shows the relevant energies for the separate systems on the left and the energies of each doubly dressed states in the combined system on the right. The infinite ladder of doubly dressed states are each separated from their neighbor by the energy $\hbar\delta$ and correspond to a switch in the atomic state. These states correspond to the manifold states discussed in Sec. 1.5.

model [38, 39] and the doubly dressed atom picture [40, 41]. For brevity, we will only discuss the doubly dressed atom picture. The derivations will primarily follow those in Ref. [31].

Sec. 1.5 discusses the dressed atom technique for understanding for the atom-light system together, rather than as two separate entities. We will again employ this technique, but now we use it for both optical frequencies.

Of particular note, there are no longer just two states within the manifold as described earlier. As seen in Fig. 2.3, we can identify an infinite ladder of states, each separated by $\hbar\delta$. Each state is connected to the adjacent state by only one of the light fields. The

states are therefore coupled by the Rabi frequency of that field, $\Omega_{r,b}$, allowing us to write the Hamiltonian as an infinitely extending matrix:

$$\mathcal{H} = \frac{\hbar}{2}\begin{pmatrix}
\ddots & & & & & & & & \\
\Omega_b & +3\delta & \Omega_r & 0 & 0 & 0 & 0 & 0 & 0 \\
0 & \Omega_r & +2\delta & \Omega_b & 0 & 0 & 0 & 0 & 0 \\
0 & 0 & \Omega_b & +\delta & \Omega_r & 0 & 0 & 0 & 0 \\
0 & 0 & 0 & \Omega_r & 0 & \Omega_b & 0 & 0 & 0 \\
0 & 0 & 0 & 0 & \Omega_b & -\delta & \Omega_r & 0 & 0 \\
0 & 0 & 0 & 0 & 0 & \Omega_r & -2\delta & \Omega_b & 0 \\
0 & 0 & 0 & 0 & 0 & 0 & \Omega_b & -3\delta & \Omega_r \\
 & & & & & & & & \ddots
\end{pmatrix}. \tag{2.9}$$

Because the light beams are independent standing waves, there are two important details to note. First, the Rabi frequencies will vary spatially, meaning what we need to consider is actually $\Omega_{r,b} \to \Omega_{r,b}(z)$. Second, because the standing waves are independent, the relative phase can be chosen. For integer multiples of π, $\Omega_r(z) = \Omega_b(z)$, but for all other phases, $\Omega_r(z) \neq \Omega_b(z)$. This will result in positions where $\Omega_r(z) = 0$, $\Omega_b(z) \neq 0$ and similarly positions where $\Omega_r(z) \neq 0$, $\Omega_b(z) = 0$.

As we discussed in Sec. 1.4 and 1.5, as the coupling Rabi frequency increases the energy separation between the two levels increases. Because the couplings alternate between each pair of states and there can be positions where one field is at zero Rabi frequency while the other is nonzero, this allows for the light shift to increase the separation between every other pair of states.

Fig. 2.4 shows an example of this for the relative phase of $\pi/4$. As the intensity of the

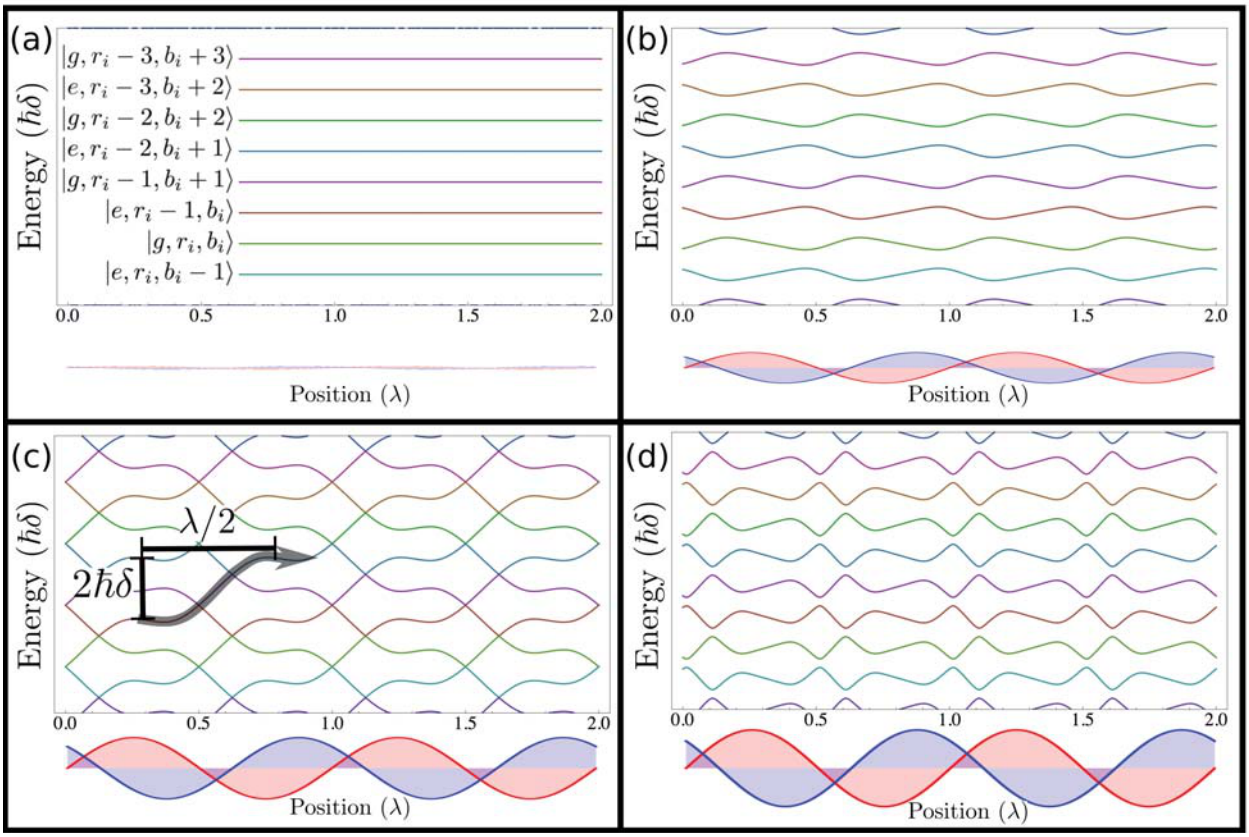

Figure 2.4: The lower portion of each image shows the bichromatic standing waves at a relative phase difference of $\pi/4$ for the Rabi frequencies (a) $\Omega_{r,b} = 0$, (b) $\Omega_{r,b} = \frac{1}{2}\sqrt{\frac{3}{2}}\delta$, (c) $\Omega_{r,b} = \sqrt{\frac{3}{2}}\delta$, (d) $\Omega_{r,b} = \frac{5}{4}\sqrt{\frac{3}{2}}\delta$. The upper portion of each image displays the spatial dependence of the eigenenergies of the dressed states due to the light shift. From [31].

light fields increases (and hence the Rabi frequency increases), the separations grow larger. When the Rabi frequency reaches $\Omega_r = \Omega_b = \sqrt{\frac{3}{2}}\delta$, the separation will cause exact crossings at nodes of the light field. Increasing the intensity beyond this point will break the exact crossings.

As an atom traverses the light fields, it can smoothly move between states, gaining or losing energy as it moves. This can be viewed as a set of potential energy surfaces. This

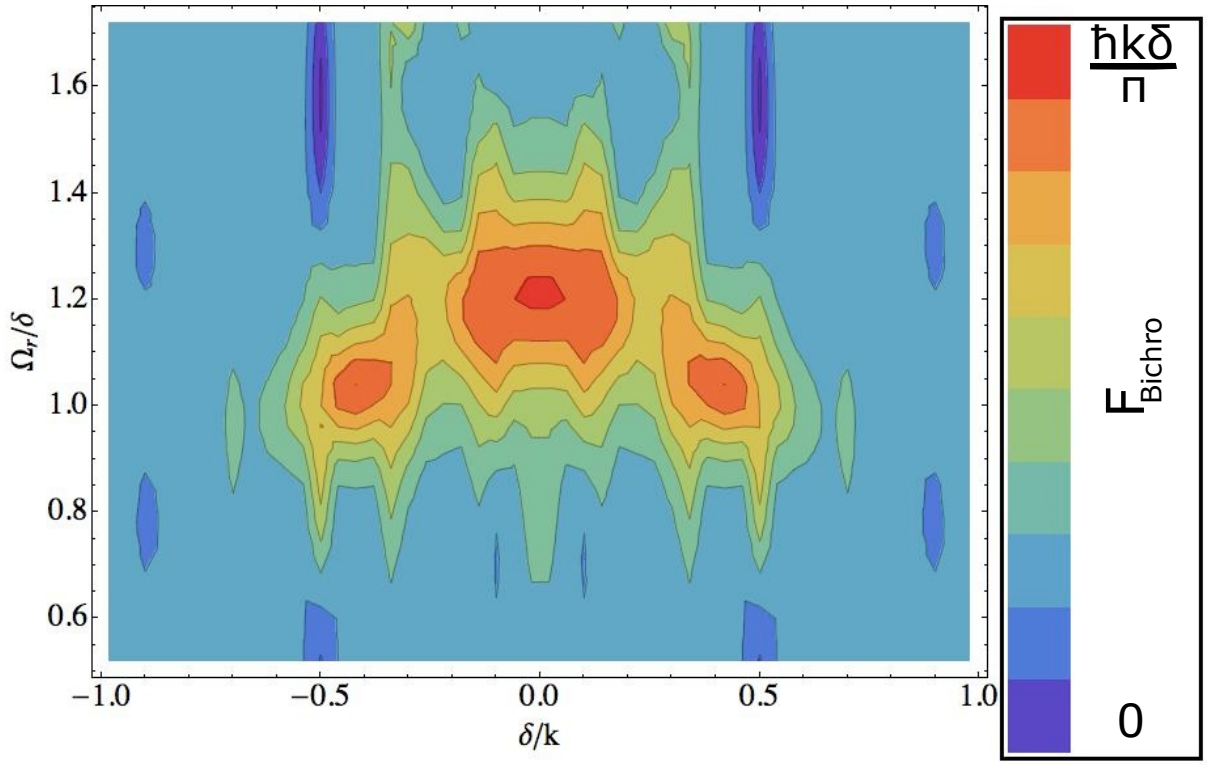

Figure 2.5: Numerical calculations of the optical Bloch equations (OBE's) for the bichromatic force with relative phase $\pi/4$. Scaled to the theoretical maximum force. From [42].

allows us to directly calculate the force [40]:

$$F_{Bichro} = -\frac{dE}{dz} \approx -\frac{\Delta E}{\Delta z} = -\frac{2\hbar\delta}{\lambda/2} = -\frac{2\hbar k\delta}{\pi}. \tag{2.10}$$

As an atom is accelerated, the amount of time it spends in a given state decreases. As $\Delta E \Delta t \rightarrow \hbar$, the probability of the atom experiencing a Landau-Zener transition increases [27]. While the velocity limit will vary depending on the choice of phase, the force is expected to break down between $\delta/4k$ and $\delta/2k$.

Exact numerical calculations of this can be made with the OBE's, with both the atom's velocity and the Rabi frequency expressed in terms of δ, as seen in Fig. 2.5. For a particular

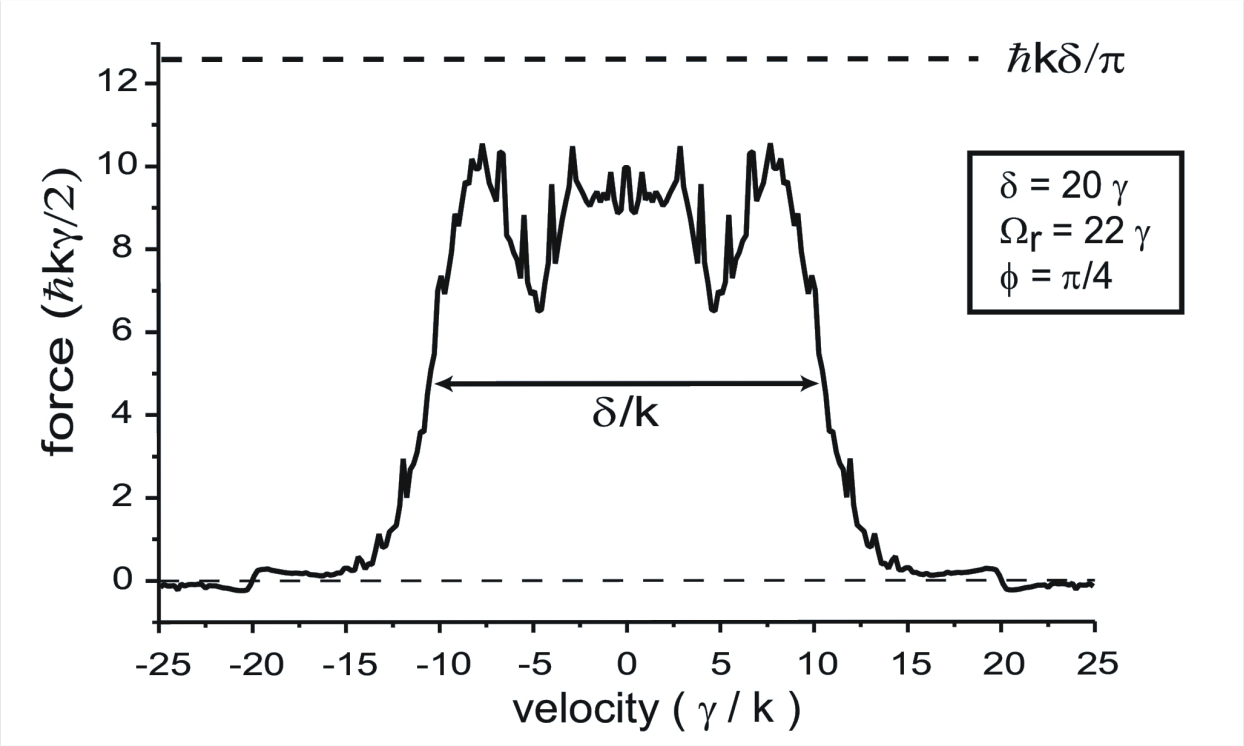

Figure 2.6: Numerical calculations of the OBE's for the bichromatic force with relative phase $\pi/4$. The force is scaled in units of the radiative force and the velocity is scaled in units of the capture velocity of the radiative force. The theoretical maximum force is shown at the top. From [43].

Rabi frequency ($\Omega_{r,b} = 1.1\delta$), we can see the velocity dependence in Fig. 2.6.

Depending on the choice of δ, the bichromatic force magnitude and velocity capture range can both be orders of magnitude stronger than the radiative force.

2.4 Other Polychromatic Forces

To move further into polychromatic forces, Ref. [44] presents a four color optical force built on the groundwork of the bichromatic force. The two additional frequencies are third harmonics of the original bichromatic detunings. The force is increased by nearly 50%, the velocity range is extended by a factor of 3, and the excited state fraction is reduced from

41% to 24%.

It is conceivable that other new and interesting optical forces can be formed by carefully selecting and adding even more frequencies. The other extreme of this is to consider a frequency sweep. Chap. 3 will contain a full discussion of the ARP force but it should also be noted that it belongs to a family of frequency sweep schemes [45]. An alternate but similar application is sawtooth-wave adiabatic passage (SWAP) cooling [46, 47].

Any kind of pulsed light is necessarily composed of multiple frequencies, so optical forces deriving from such light can also be viewed as polychromatic [25]. These pulsed schemes can take many forms as seen in Ref. [48–50]. These pulsed schemes help to bridge the expansive gap between the one, two, or four frequency forces and the frequency swept forces. One could even argue that the four discrete frequencies of Ref. [44] produce pulses by Fourier synthesis.

Chapter 3

Theory of Adiabatic Rapid Passage

Adiabatic rapid passage (ARP) is well known in the magnetic resonance community [51] for inverting the population of a two-level system. It was later shown to be a useful technique in the optical realm as well [52, 53]. This thesis focuses on using alternating ARP pulses to excite atoms and then stimulate emission to exchange $2\hbar k$ momentum per cycle. $F_{ARP} = 2\hbar k/T$ can be much larger than $F_{Rad} = \hbar k\gamma/2$ when the repetition rate of the cycles is $1/T \gg \gamma$.

3.1 Adiabatic Rapid Passage

In Sec. 1.5, we discussed the dressed atom Hamiltonian for a two-level system. We can use this formalism to describe the ARP process [54–56]. By shifting the zero energy, we can rewrite Eqn. 1.27 as

$$\mathcal{H} = \frac{\hbar}{2}\begin{pmatrix} \delta(t) & \Omega(t) \\ \Omega^*(t) & -\delta(t) \end{pmatrix}. \tag{3.1}$$

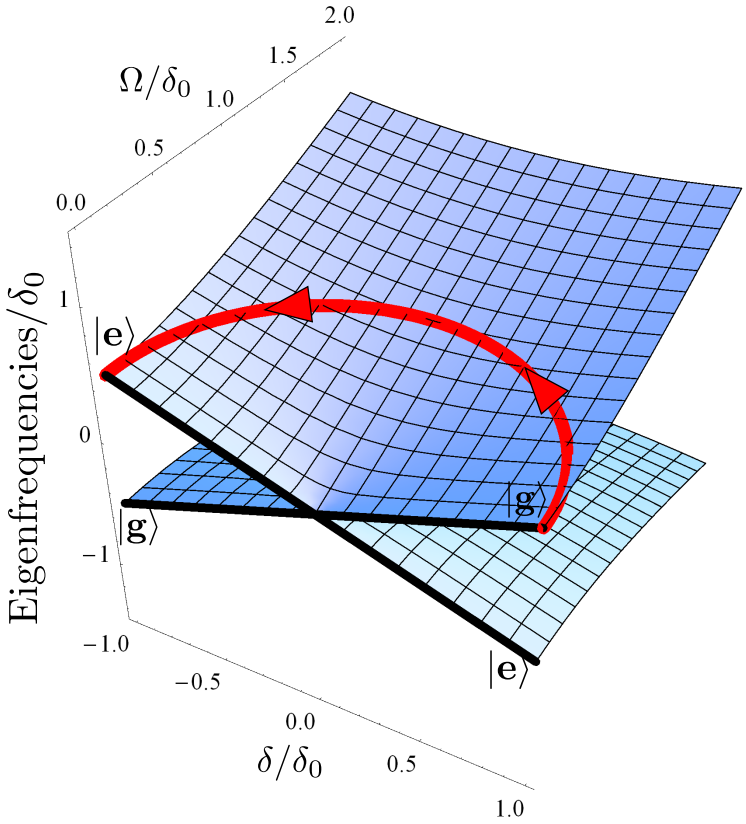

Figure 3.1: Eigenenergy sheets for a dressed two-level atom. When $\Omega(t) = 0$, the dressed states resolve to the bare atomic states. Of particular note is that the upper sheet changes from $|g\rangle$ to $|e\rangle$ as δ changes sign. The curved path shows one possible pathway for the ARP process.

We can again diagonalize this to find the eigenenergies to be

$$E_{\pm}(t) = \pm\frac{\hbar}{2}\sqrt{|\Omega(t)|^2 + (\delta(t))^2}. \tag{3.2}$$

To better understand the eigenstates, we can plot the eigenenergies for both Rabi frequency and detuning as in Fig. 3.1. As we discussed in Sec. 1.5, the mixing of the atomic states increases as the Rabi frequency increases. So as $\Omega \to 0$ the eigenstates approach the atomic states. In this limit, we can see that the detuning determines which of the states

($|g, N\rangle$ and $|e, N-1\rangle$) has a higher energy. This can be seen more clearly in Fig. 3.1.

A synchronized sweep of both Rabi frequency and detuning allows an adiabatic transition from ground state to excited state while remaining within a chosen eigenstate. Fig. 3.1 shows the trajectory of a chosen sweep: $\delta(t) = \delta_0 \cos(\omega_m t)$ and $\Omega(t) = \Omega_0 \sin(\omega_m t)$ from 0 to π/ω_m where $\omega_m = 2\pi \times 160$ MHz is the experimentally chosen modulation frequency. We can also sweep along the lower eigenstate using $\delta(t) = -\delta_0 \cos(\omega_m t)$. By following the instantaneous frequency, we refer to these choices of frequency sweep as sweeping down and sweeping up, respectively.

To use these synchronous Rabi frequency and detuning sweeps to move an atom in the excited state back into the ground state, the Rabi frequency sweep remains the same, but now for the detuning, sweeping up occurs on the higher eigenstate and sweeping down occurs on the lower eigenstate.

Another method for understanding the ARP process is to make use of the Bloch sphere model [2, 3, 57] discussed in Sec. 1.3. As shown earlier in Eqn. 1.18, the time dependence of the Bloch vector is controlled by the torque vector. The synchronous sweep of Rabi frequency and detuning describes the movement of the torque vector.

For a sweep up ($\delta(t) = -\delta_0 \cos(\omega_m t)$), the torque vector begins by pointing at the south pole and moves along a meridian, ultimately pointing at the north pole. For a sweep down, the torque vector's path would be reversed. For both frequency sweep directions, the Rabi frequency ($\Omega(t) = \Omega_0 \sin(\omega_m t)$) starts at 0, increases to a maximum when $\delta(t) = 0$, and finally returns to 0. This synchronous sweep moves the Bloch vector from the south pole (ground state) to the north pole (excited state).

The adiabaticity of this process can be quantified as

$$|\overrightarrow{\Omega}(t)| \gg \left|\frac{d\theta}{dt}\right| \tag{3.3}$$

where the mixing angle $\theta(t)$ is defined [51, 58–60][1] as

$$\theta(t) \equiv \arctan \frac{\delta(t)}{\Omega_0(t)}. \tag{3.4}$$

$\theta(t)$ is the angle between the torque vector and the north pole. The rapidity of this process requires that the entire process occurs significantly faster than the natural relaxation process of the system, $100\gamma \approx \omega_m = 2\pi \times 160$ MHz for our particular experiments.

If the sweep is too fast, the Bloch vector does not follow the torque vector adiabatically, leaving a fraction of the population not inverted at the end of the sweep. In the dressed atom picture, there is some probability of a non-adiabatic transition to the opposite manifold state during the sweep, similar to a Landau-Zener transition. This non-adiabatic transition probability, P_{nad}, does not have an exact analytical solution and is explored further in Ref. [58].

3.2 ARP Force Sequence

In Sec. 3.1, we discussed the theory behind a single ARP sequence to move an atom from the ground state to the excited state. As discussed in the beginning of Chap. 2, this absorption also results in a change of momentum equal to $+\hbar\overrightarrow{k}$. The ARP process is also able to move an atom from the excited state back to the ground state. The recoil from stimulated emission results in a change of momentum equal to $-\hbar\overrightarrow{k}$.

By continually sending ARP pulses in the same direction, these momentum changes would cancel each other out. As seen in Fig. 3.2, by alternating the direction of the pulses, the atom would absorb light from one direction and be stimulated to emit light into the opposite direction, thereby receiving a net of $2\hbar\overrightarrow{k}$ per two pulse cycle.

[1]Note that some sources [6, 33, 45] prefer to use the phase angle (confusingly also labeled $\theta(t)$) defined $2\theta(t) \equiv \arctan \frac{\Omega_0(t)}{\delta(t)}$ in Eqn. 3.3 to quantify adiabatic conditions. $|\dot{\theta}(t)|$ is nearly identical for both definitions

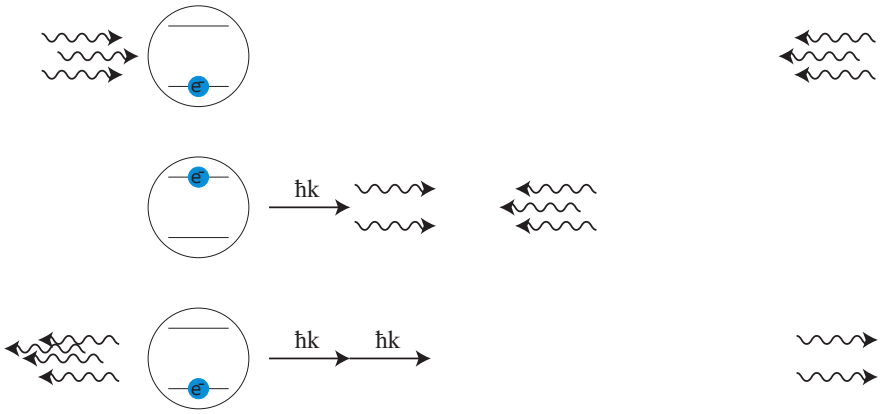

Figure 3.2: Generalized Schematic for the ARP force. An atom begins in the ground state. An ARP pulse from the left causes absorption; exciting the atom and imparting $\hbar k$ momentum. An ARP pulse from the right causes stimulated emission; returning the atom to the ground state and imparting another $\hbar k$ momentum change in the same direction as the first.

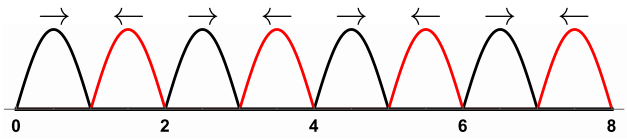

Time (π/ω_{m})

(a) ARP sequence with alternating pulses.

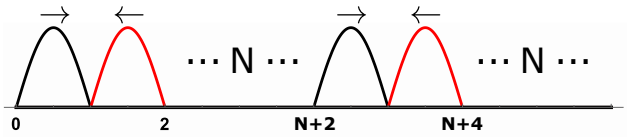

Time (π/ω_{m})

(b) ARP sequence with a dead time of N pulses.

Figure 3.3: The ARP process relies on alternating light pulses to excite and stimulate emission. A spontaneous emission event will reverse the direction of the force. Part (a) shows the timing scheme that would be ideal without spontaneous emission. Part (b) shows a syncopated timing scheme including a dead time of N pulses. Under such an asymmetry, the desired sequence of a left pulse to excite and a right pulse to stimulate will spend less time in the excited state per pulse pair than the undesired sequence of right pulse to excite and left pulse to stimulate. This statistically favors correction to return to the desired sequence and therefore allows for a preferred force direction.

Unfortunately, even though an individual ARP process can be much faster than the spontaneous decay rate, for a large enough number of pulses, spontaneous decay will need to be accounted for. A single spontaneous decay would reverse the ARP cycle: pulses intended to be absorbed would now stimulate emission and vice versa. This would also reverse the net momentum change per two pulse cycle and thus reverse the force.

One possibility for addressing this concern is to introduce "dead time", a period of time without light between the pairs of pulses. Fig. 3.3 shows two examples of timing configurations for the ARP force. In Fig. 3.3a, there is no dead time and each pair of pulses is immediately followed by another pair. This is ideal for keeping the repetition rate high, but each spontaneous emission event would reverse the direction of the force, causing the net force to approach 0.

Fig. 3.3b shows a configuration in which there are N periods of π/ω_m dead time between successive pairs of pulses. While the atom is experiencing a force in the intended direction, the second pulse (pictured in red) will return the atom to the ground state and the atom will remain there during the dead time. Spontaneous emission will still result in a reversal of the force, but now, when the second pulse excites the atom, the dead time extends the time spent in the excited state per two pulse cycle. This allows for the greater probability of another spontaneous emission event, which would correct the force direction.

Fig. 3.4 shows the ARP force vs number of pulses pairs for five different values of dead time in increments of π/ω_m from Ref. [57]. The zero dead time configuration quickly approaches an average force of zero, but the non-zero dead time configurations are able to sustain a consistent average force over many pulse pairs. From this, we have chosen to use a dead time of $2\pi/\omega_m$ because it sustains the largest average force after many pulse pairs.

Only considering the statistical nature of the dead time, the asymptotes of Fig. 3.4 can

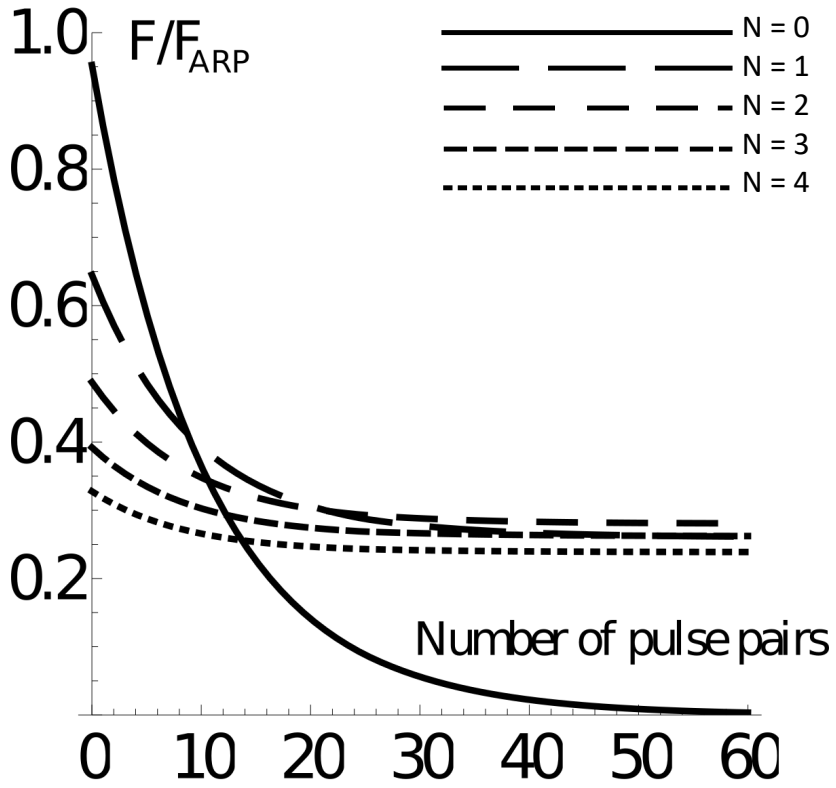

Figure 3.4: The calculated force *vs.* number of pulse pairs for various length of dead time. The solid curve shows the case of no dead time, and the dashed curves show the cases for different values of dead time. As the dashes get smaller, the length of dead time increases in integer multiples of π/ω_m (1, 2, 3, and 4 respectively). For a large number of pulse pairs the force converges to a non-zero value with the inclusion of dead time. For the experiment the value of $N = 2\pi/\omega_m$ is chosen. Adapted from [57].

be calculated to be

$$F_{ARP,spont} = \frac{\hbar k \omega_m}{\pi} \frac{2N}{(N+2)^2}. \tag{3.5}$$

Unfortunately, this only serves as an approximation. Ref. [58] defines an additional reduction term $\kappa(1 - \sqrt{P_{nad}})$ where κ is a complicated function of the non-adiabatic transition

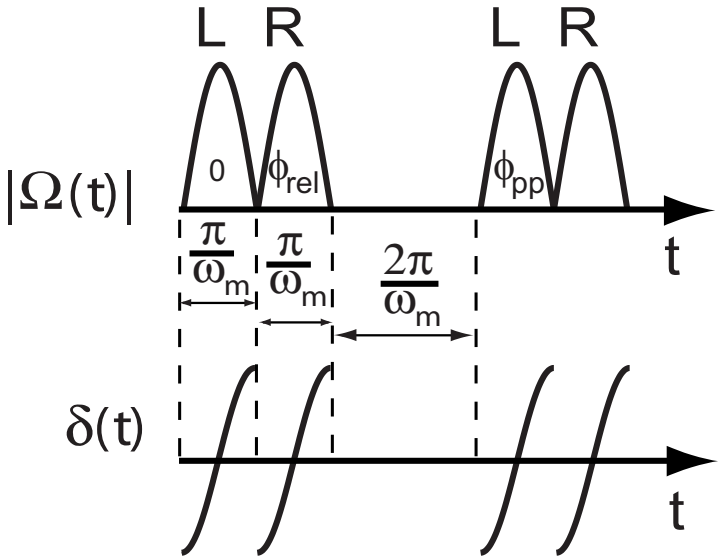

Figure 3.5: The timing schematic for our experiments. The synchronous sweeps are defined by $\delta(t) = -\delta_0 \cos(\omega_m t)$ and $\Omega(t) = \Omega_0 \sin(\omega_m t)$ from 0 to π/ω_m where $\omega_m = 2\pi \times 160$ MHz. We can alternatively use the chirp $\delta(t) = \delta_0 \cos(\omega_m t)$ (not pictured).

probability, P_{nad}. This results in a force of

$$F_{ARP,spont} = \kappa\left(1 - \sqrt{P_{nad}}\right)\frac{2\hbar k\omega_m}{\pi(2+N)}. \tag{3.6}$$

Generally, $\kappa \approx 1/2$ is slightly larger for small P_{nad} and slightly smaller for large P_{nad}.

It should be noted that introducing this dead time will affect the maximum possible force. For each ideal cycle, the atom gains $2\hbar k$ of momentum in $4\pi/\omega_m$ instead of $2\pi/\omega_m$, effectively halving the maximum possible force. Given our experimentally chosen sweep rate of $\omega_m = 2\pi \times 160$ MHz $\approx 100\gamma$, this results in a force of

$$F_{ARP,ideal} = \frac{\Delta p}{\Delta t} = \frac{2\hbar k}{4\pi/\omega_m} = \frac{\hbar k\omega_m}{2\pi} \approx \frac{100\hbar k\gamma}{2\pi} \approx 32F_{Rad}. \tag{3.7}$$

With the inclusion of spontaneous emission, the expected force is reduced further [57, 58] to

$$F_{ARP,spont} \approx 19 F_{Rad}, \tag{3.8}$$

as seen in Fig. 3.4. This result can also be obtained assuming $P_{nad} = 0$ and $\kappa = 0.6$

Fig. 3.5 explicitly shows our experimentally chosen timing for the Rabi frequency and detuning synchronous sweeps with the selected dead time of $2\pi/\omega_m = 6.25$ ns. Each pulse lasts for $\pi/\omega_m = 3.125$ ns and can either sweep up in frequency from $\omega_\ell - \delta_0$ to $\omega_\ell + \delta_0$ (pictured) or sweep down in frequency from $\omega_\ell + \delta_0$ to $\omega_\ell - \delta_0$.

3.3 ARP Force Parameters

The ARP process described in Sec. 3.1 will successfully invert the population for a wide array of parameters. Over many cycles, slightly imperfect inversions will accumulate. This can lead to low fidelity or reproducibility of further inversions and therefore reduce the average force.

Fig. 3.6 shows numerical simulations of the strength of the ARP force for an array of Rabi frequencies and chirp ranges. We call this type of image a forcemap and will refer to it again numerous times in Chap. 6. Part a is the ARP force of an individual pulse pair and part b is the ARP force averaged over 320 pulse pairs. With the increased number of pulse pairs, the ARP force is significantly more sensitive to the Rabi frequency and chirp range parameters.

The magnetic resonance community typically uses ARP in the parameter space where

$$\delta_0 \sim \Omega_0 \gg \omega_m \gg \gamma \tag{3.9}$$

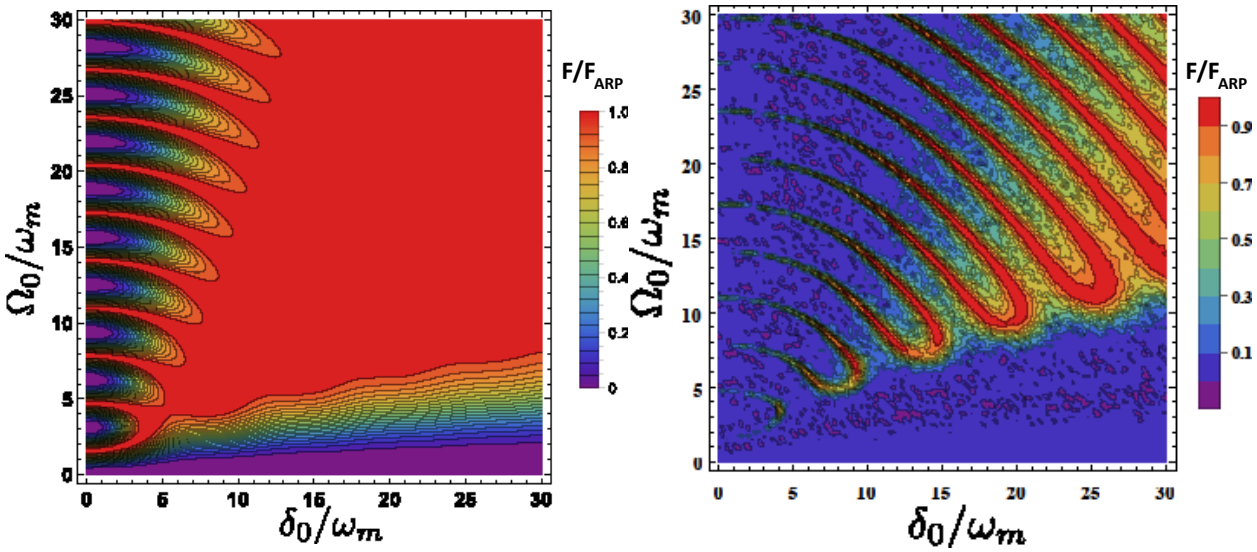

(a) 1 pulse pair. (b) 320 pulse pairs.

Figure 3.6: Numerical simulations of the ARP force as a function of Rabi frequency and chirp range. By comparing the force after 1 and 320 pulse pairs, we can observe the increased sensitivity of parameter selection. This is especially true in the lower left corner, which is the experimentally accessible region. From [33].

corresponding to the upper right area of Fig. 3.6. Given our experimental choice of $\omega_m = 2\pi \times 160$ MHz $\approx 100\gamma$, we can only access the region where

$$\delta_0 \sim \Omega_0 \sim \omega_m \gg \gamma, \tag{3.10}$$

corresponding to the lower left area of Fig. 3.6.

Our experimentally accessible region requires an especially delicate balance of Rabi frequency and chirp range. Fig. 3.7 gives two examples of the Bloch vector's movement during inversion. Part a corresponds to a trajectory within conventional parameters. Part b corresponds to a particularly selected trajectory within our experimentally accessible region. This is done to demonstrate that there are possible paths for inversion in the unconventional parameter space that we conduct our experiments in.

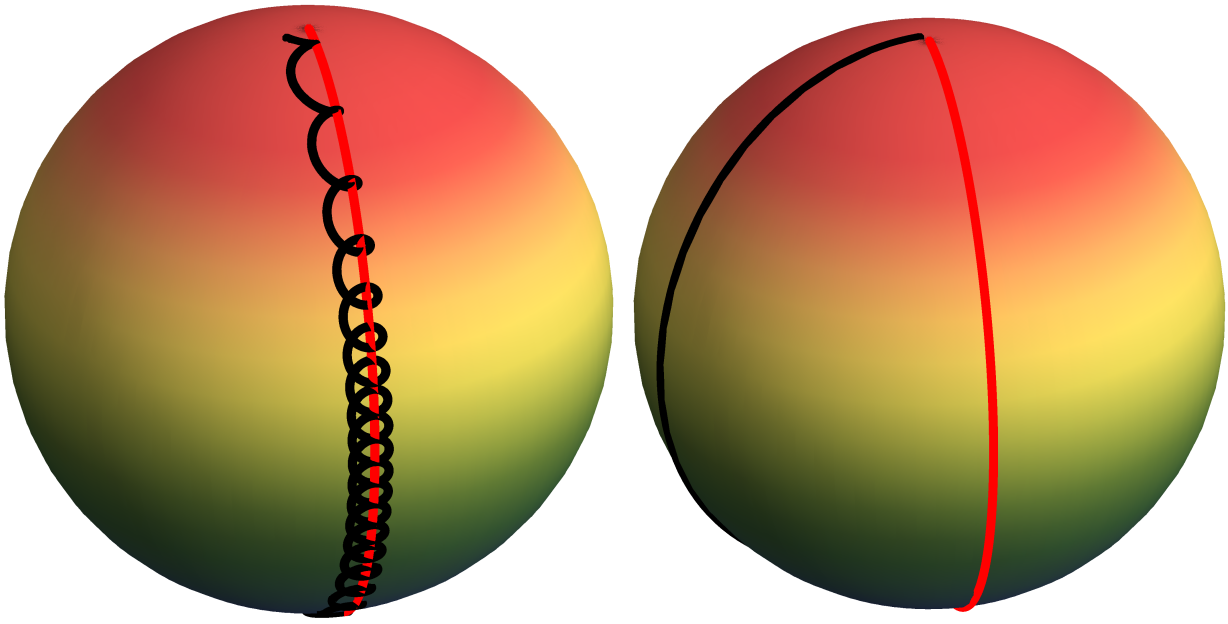

(a) $\delta_0 = 30\omega_m$, $\Omega_0 = 50\omega_m$ (b) $\delta_0 = 1.10\omega_m$, $\Omega_0 = 1.61\omega_m$

Figure 3.7: Bloch sphere representation of ARP population inversion. Part (a) displays inversion within the conventional parameter space. Part (b) displays inversion via a carefully selected Rabi frequency and chirp range within the unconventional parameter space. This was chosen to show that inversion is still possible in the more sensitive regime.

3.4 ARP on Moving Atoms

As of the writing of this thesis, theory on applying the ARP force to moving atoms has been rather sparse. Primarily this has been due to a lack of generality. Calculations for the ARP force are principally performed by numerically solving the OBE's ~ 100 times within each pulse [43]. This method will not net us a general form directly, but we can search for patterns based on the results of these calculations to build towards a general form.

The atomic velocity results in a Doppler detuning of $\pm kv$ for the counter-propagating light beams. This detuning means that the frequency sweep is no longer centered on ω_a. For very large Doppler shifts, i.e. $|kv| > \delta_0$, the frequency sweep doesn't even pass through

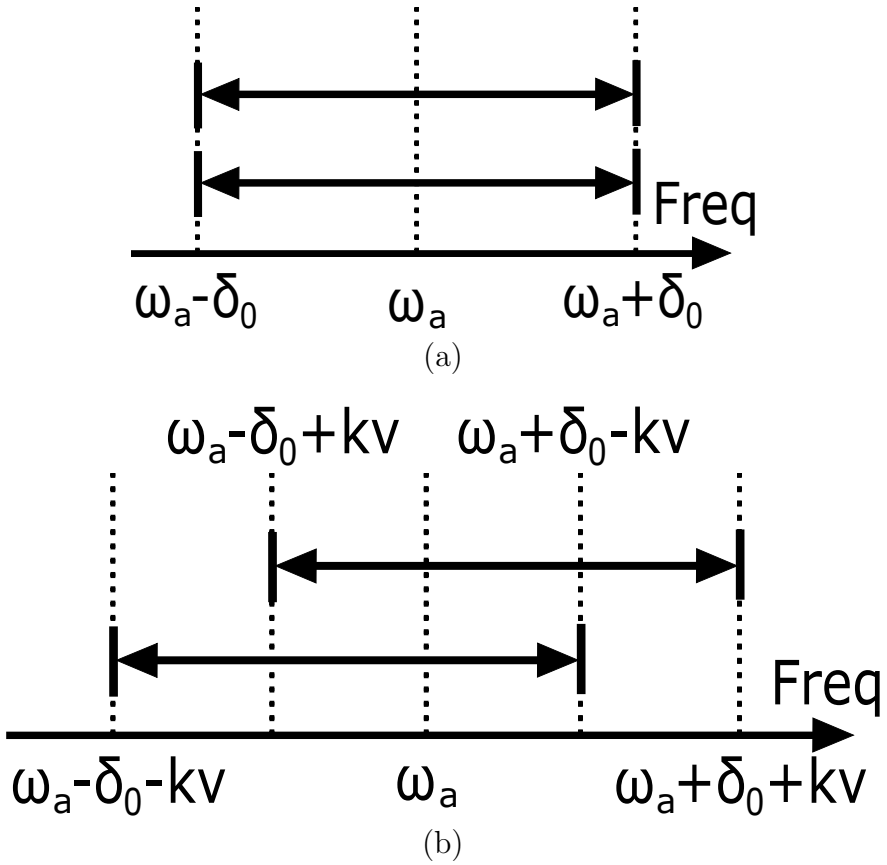

Figure 3.8: Frequency range of chirped pulses with and without Doppler shifts. As the Doppler shift increases, the center of the sweep moves progressively farther from atomic frequency.

resonance, and therefore one would can presume little chance of consistent inversion.

As seen in Fig. 3.8, as $|kv| \to \delta_0$, the center of the frequency sweep moves progressively farther from ω_a. The dressed state model shows that frequency sweeps that are asymmetric about ω_a do not fully conserve energy. This will lower the probability of inversion. Intuitively, we would guess that velocities that are a significant fraction of δ_0/k would no longer exhibit strong forces.

Fig. 3.9 shows a calculation of the velocity dependence for a selection of parameters for Rabi frequency and chirp range from Ref. [43]. This calculation uses the "dragged

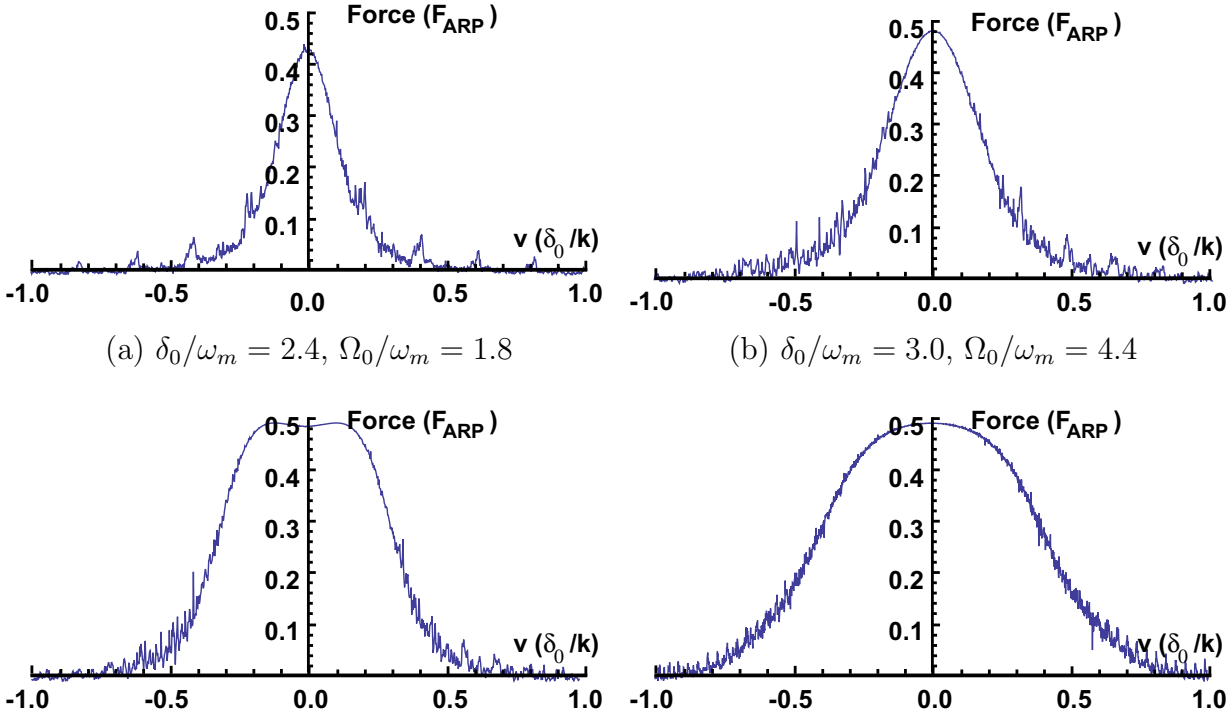

(a) $\delta_0/\omega_m = 2.4$, $\Omega_0/\omega_m = 1.8$

(b) $\delta_0/\omega_m = 3.0$, $\Omega_0/\omega_m = 4.4$

(c) $\delta_0/\omega_m = 4.19$, $\Omega_0/\omega_m = 3.39$

(d) $\delta_0/\omega_m = 14$, $\Omega_0/\omega_m = 18$

Figure 3.9: Numerical simulations of the velocity dependence using the "dragged atom approach". The horizontal axes are adjusted to help elucidate generalized patterns in the velocity dependence. From [43].

atom approach" in which the atomic velocity is kept fixed throughout the calculation. For very short interaction times, this should sufficiently represent the ARP force. For longer interaction times (including those described in this thesis), it will fall short, but we can still gain some useful information.

Examining Fig. 3.9, there is no simple fraction of δ_0/k to determine the velocity where the force is reduced. As δ_0 and Ω_0 increase, so too does the fraction of δ_0/k at which the force is reduced.

I do want to note that the particular parameters chosen for Fig. 3.9 were specifically chosen by the authors of Ref. [43] to match the work of Ref. [61]. As we saw in Fig. 3.6,

many parameters will yield very small forces at $v = 0$. Not all choices of δ_0 and Ω_0 will share the features seen in Fig. 3.9.

Chapter 4

Metastable Helium Apparatus

In this chapter, we will discuss the vacuum system used in our experiments. It is comprised of 3 major sections: metastable helium source, interaction region, and detection chamber as seen in Fig. 4.1.

4.1 Metastable Helium Source

The first section of our vacuum system is devoted to the metastable helium source. This region can be pumped in two different configurations.

While the source is off, the region is pumped by a Pfeiffer Balzers TPH 330 turbo pump, backed by a Pfeiffer Duo 110 mechanical pump. This keeps the pressure in the vacuum system $\sim 10^{-6}$ Torr, with backing pressure $\sim 10^{-3}$ Torr.

With the source on, there is a large flux of helium into the system. To remove most of the helium, we open a valve to an additional Welch 1376 attached to the 'He out' port shown in Fig. 4.1. This helps to define the helium flow within the chamber as well as relieve some of the pumping burden off of the TPH 330. While the source is on, pressure in the chamber

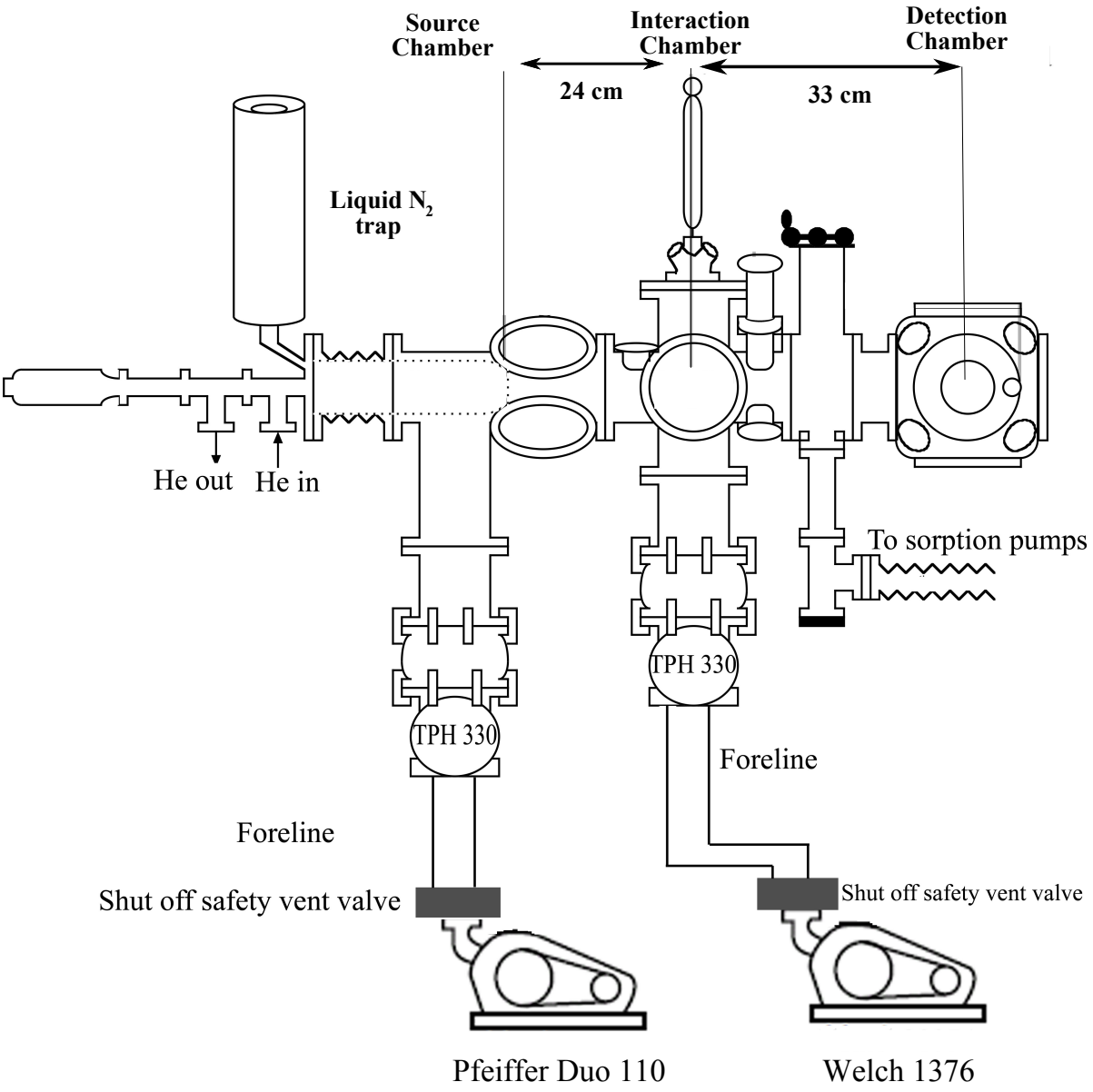

Figure 4.1: Schematic of the vacuum system used in the ARP experiments.

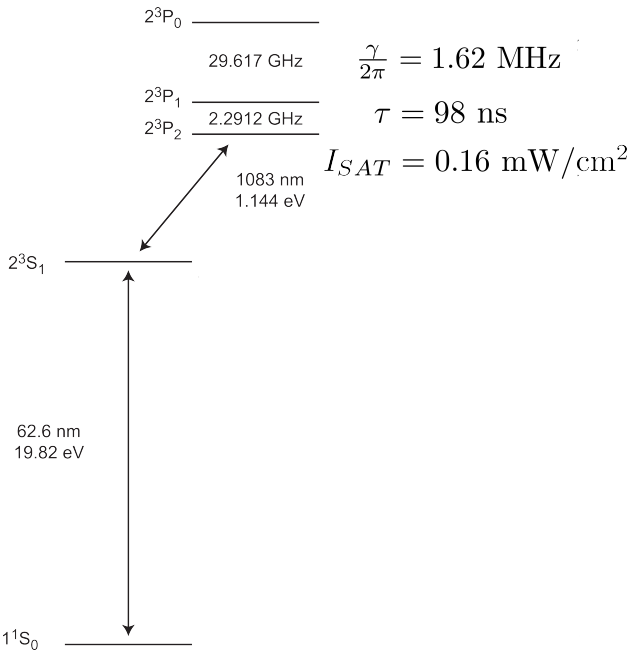

Figure 4.2: Relevant energy levels for the ARP experiments in helium. The lifetime of the metastable state 2^3S_1 is $\sim$ 7900s and serves as the "ground state" for our experiments [62].

is $\sim 10^{-5}$ Torr, with backing pressure ~ 0.2 Torr.

In our experiments, we focus on the 1083.33 nm $2^3S_1 - 2^3P_2$ transition in He. The lower state, 2^3S_1 is, in fact, not a true ground state of the atom, but rather a metastable state (He*), existing 19.82 eV above the true ground state of the atom, 1^1S_0, as seen in Fig. 4.2. Because $2^3S_1 - 2^3P_2$ requires $\Delta J = +1$, it is ideal for optical pumping to create a closed transition, as seen in Fig. 4.3. Before our primary experiment, the atoms experience an optical pumping stage of $\sim$ 1 μs which allows for $\sim$ 5 cycles. Given an even initial distribution, we can expect $\sim 97\%$ of the atoms to be in the $m_j = +1$ ground state.

Transition of He* to the true ground state is doubly forbidden by selection rules; transition of our excited state 2^3P_2 to the true ground state is singly forbidden, therefore spontaneous emission will generally return the atom to the metastable state.

Optically exciting atoms into the metastable state would be foolishly difficult. Instead,

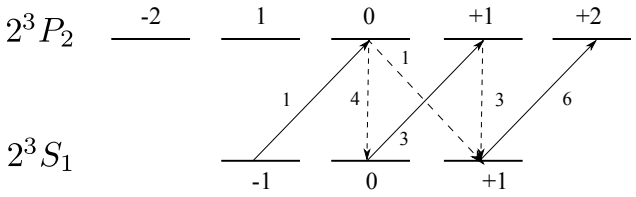

Figure 4.3: Relative transition rates between magnetic sublevels of the $2^3S_1 \rightarrow 2^3P_2$ transition in metastable helium. The solid lines are the allowed transitions for σ^+ polarized light. Spontaneous decay can occur randomly along either solid or dashed lines. Over time, the population in the $m_j = +1$ ground state will increase as the population in the $m_j = -1$ and $m_j = 0$ ground states decrease.

we achieve this via a discharge using reverse backflow as shown in Fig. 4.4. This source was originally designed by Shimizu [63] with revisions by Mastwijk *et al.* [64]. More details can be found in [65].

He flows into the vacuum system and between the outside of a hollow glass tube and a liquid nitrogen cooled stainless steel jacket. Inside of the glass tube is a tungsten needle at ~ -2100 V. When the He arrives at the tip of the glass tube, it meets the electric discharge from the tungsten needle which ionizes the atoms. When electrons recombine with the positive ions, most will return to the true ground state via collisions, but a small fraction ($\sim 10^{-5}$) will remain in our desired state.

While He is flowing into the system, we open access between a roughing pump and the back end of the glass tube. This pulls most of the He out of the vacuum system. Because of the narrow opening of the nozzle plate and the high flow rate of helium entering the system, we do not have to worry about exposing roughing pump to the high vacuum created by the turbo pump in the source chamber.

Behind the nozzle plate is a 0.5 mm aperture on a skimmer plate. This aperture establishes differential pumping between the two chambers as well as defining the atomic beam as it enters the interaction chamber (also sometimes referred to as the beam chamber).

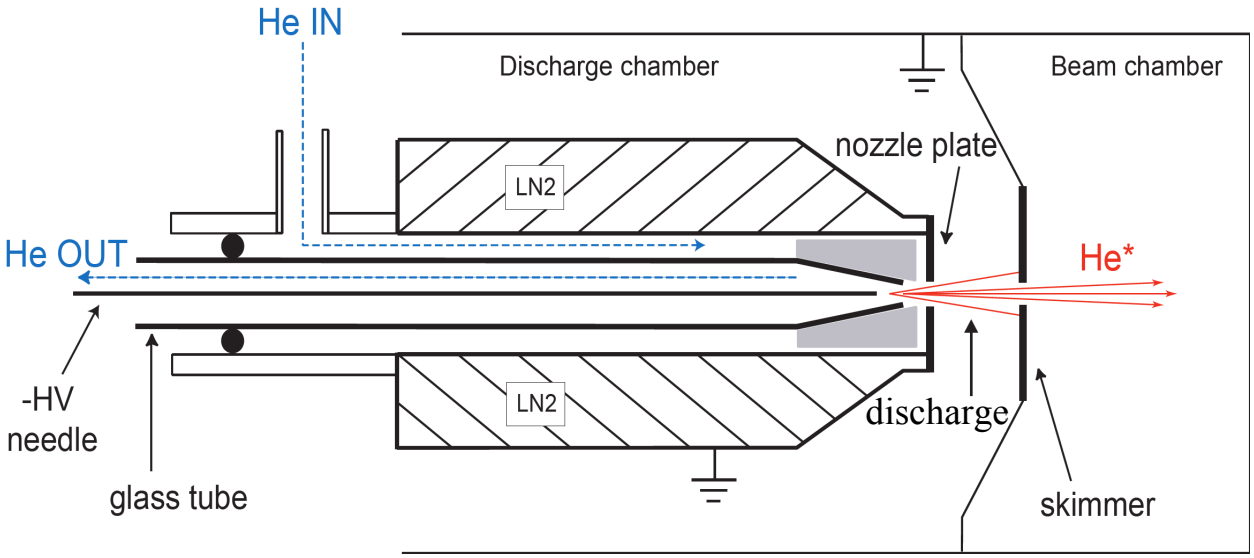

Figure 4.4: A schematic showing production of He* via reverse backflow discharge. The discharge is created by ~ -2100 V applied to the tungsten needle. From [43].

4.2 Interaction Chamber

The next section of our vacuum system is the interaction chamber. This chamber is pumped by a Pfeiffer Balzers TPH 330 turbo pump, backed by a Welch 1376. This keeps the pressure in the vacuum system $\sim 10^{-6}$ Torr, with backing pressure $\sim 10^{-3}$ Torr.

The He* beam passes through the aperture in the skimmer plate and into the interaction region. The longitudinal velocity distribution of the atoms is a Maxwellian with average velocity of ~ 1000 m/s and half width of ± 400 m/s.

24 cm away from the skimmer plate, we have a slit mounted to the front of a pair of Helmholtz coils as seen in Fig. 4.5. The slit is 1 cm tall and 250 μm wide, serving to constrain the transverse velocity of the helium beam to ± 1 m/s.

The Helmholtz coils are mounted on a machinable glass-ceramic Macor mount (see Fig. 4.5b). The coils serve to provide a uniform magnetic field transverse to the atomic beam. The laser light used in our experiments will travel approximately through the center

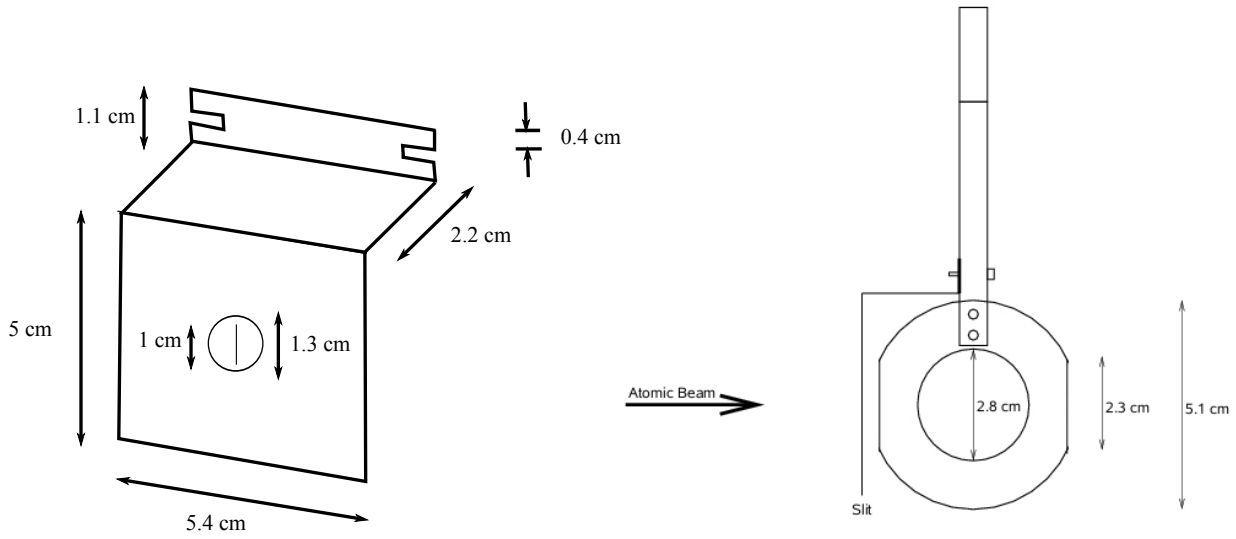

(a) Front View (b) Side View

Figure 4.5: Part (a) shows a schematic of the slit for the atomic beam. A thin slit is cut into a metal foil that is glued on a piece of aluminum. The slit is 1 cm tall and 250 μ wide. Part (b) shows a side-view of the Helmholtz coils including mount and slit for the atomic beam. Both the optical pumping light and the ARP light will travel through the coils, perpendicular to the page with a variable separation usually ~ 5 mm.

of the coils and use this co-linear magnetic field to define a z-axis.

The field also breaks the Zeeman degeneracy of the 2^3S_1 state. Only a few Gauss are needed to break this degeneracy, $(1.4\ \text{MHz/G})\mathbf{B} > \gamma/2\pi = 1.62$ MHz. The coils are designed for $\mathbf{B} = 3.77\times$I (amps), so this is easy to achieve with only a few amperes of current.

4.3 Detection Chamber

The final chamber in our vacuum system is the detection chamber. This chamber is physically connected to the interaction chamber via a gate valve and its low pressure is achieved by this open connection.

When the gate valve is closed, this chamber can be opened for maintenance without

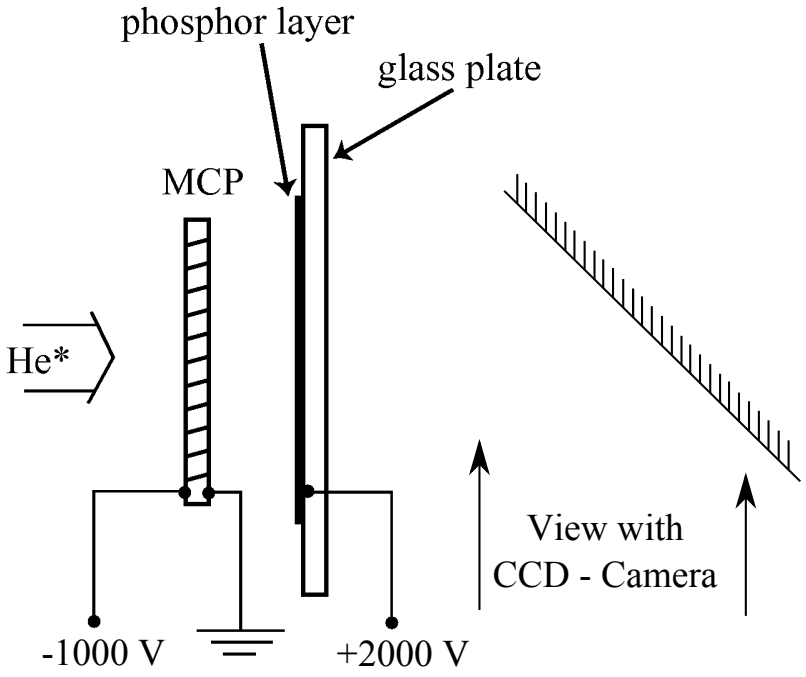

Figure 4.6: Diagram of the MCP/PS detector. He* incident on the MCP causes electrons to be ejected. The bias across the MCP cause a cascade of electrons to be accelerated to the phosphor screen, where the fluorescence of the phosphor can be seen. A CCD camera is then used to capture images of the screen. Modified from [43].

having to turn off the turbo pumps in the other regions of the vacuum system. After maintenance is finished, sorption pumps can be used to bring the detection chamber to $\sim 10^{-3}$ Torr. At this pressure, we can slowly open the gate valve to reintroduce this region to the $\sim 10^{-6}$ Torr provided by the turbo pump in the interaction region without overwhelming the turbo pump.

After atoms pass through the slit and Helmholtz coils in the interaction region, they travel approximately 33 cm to our He* detector (Fig. 4.6). He* atoms carry almost 20 eV of internal energy which can be released by collision. We can take advantage of this by using a micro-channel plate (MCP). The Photonis MCP 25/12/10/12 D 40:1 used in our detector is a thin, 1" diameter disk comprised of 10 μm diameter, lead-coated glass tubes (channels)

arranged in a hexagonal lattice with a 12 μm lattice spacing. These channels are aligned at an angle of 8° from the normal of the plate.

The large internal energy of the He* atom incident on the MCP is more than enough to eject an electron into the channel it struck. We apply a large negative bias (~ -1000V) on the front of the plate and ground the rear surface. This causes the electrons in each channel to accelerate and collide with the channel walls, ejecting yet more electrons. This multiplication is highly dependent on bias voltage. The Photonis MCP's used in our experiment provide a gain of $\sim 10^4$ for a bias voltage of -1000 V.

As shown in Fig. 4.6, the MCP is followed immediately by a phosphor screen (PS). The PS is a glass plate with a thin coating of indium tin oxide (ITO) and aluminum for conductivity, underneath a layer of P43 phosphor. The electrons are accelerated towards the screen by $\sim +2000$ V bias voltage. Electrons impacting the screen cause fluorescence of the phosphor at the point of impact. The brightness is roughly proportional to the electron flux. This allows for the brightness at a given point to be related to the number of He* atoms incident on the MCP channel directly in front of that given point. This allows for position sensitive detection of He*.

Although there is a relation between He* flux and brightness, the MCP/PS does have a nonlinear response as well as non-uniformity of the phosphor layer caused by over-exposure of the screen and degradation of the MCP.

While our detector design allows for high efficiency detection of He*, it also allows for high efficiency detection of UV light emitted by the source. Since the UV and He* have similar paths to the detector, the two are indistinguishable. Luckily, He* that interact in our experiment will be given new transverse velocities, most of which will land on a part of the detector that the UV light is unable to reach.

Finally, a mirror is mounted at 45° to allow for recording the image of the phosphor screen

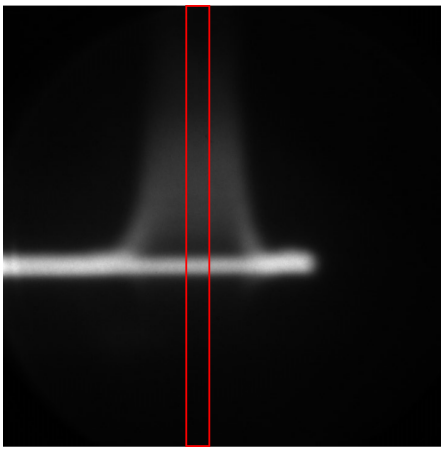

(a) Phosphor Screen Image

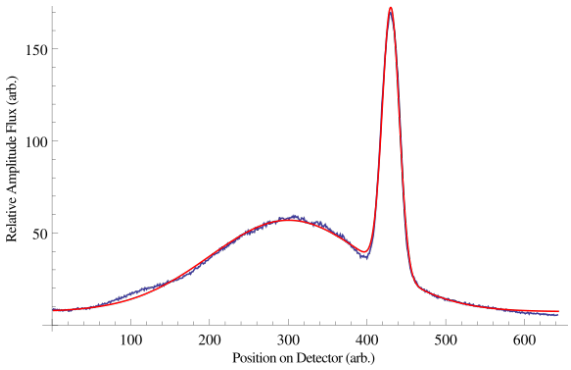

(b) Phosphor Screen Lineout

Figure 4.7: Part (a) shows a rotated CCD image of the phosphor screen while atoms are being deflected. The red box illustrates the area of interest. We horizontally average the intensity in this box. Part (b) shows the resulting lineout in blue with a fit to the data in red.

by an external CCD camera through a side window of the detection chamber. Fig. 4.7a shows an example of a phosphor screen image rotated by 90°. The atoms are deflected horizontally away from the UV background left by the source and slit. We rotate the image to present this as a vertical deflection. We define an area of interest (shown as a red box) and average the intensity over each row of pixels. Fig. 4.7 shows this average in blue and our fit in red.

We fit both the background and the deflected atoms to Gaussian profiles. Usually this fits to a high degree of accuracy. Sometimes we will alternatively use a Maxwellian profile to fit to the shape of the deflected atoms. This better mimics the longitudinal velocity profile of the atoms, but costs more computational time.

Sometimes an atom will be out of phase with the desired sequence of pulses and will not be corrected by the probabilistic spontaneous emission process. We attribute the small number of negative velocity atoms in the tail of the right-hand edge of Fig. 4.7b to this effect.

Chapter 5

ARP Light Production

In this chapter, we will discuss the production of the 1083.33 nm light used in our experiment. An overview of the system can be seen in Fig 5.1.

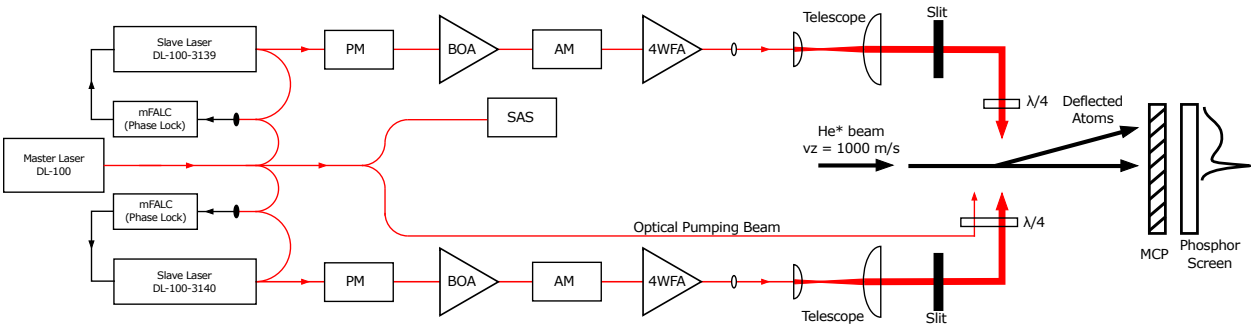

Figure 5.1: A block diagram of the major optical components for our experiment. PM - Phase Modulator, BOA - Booster Optical Amplifier, AM - Amplitude Modulator, 4WFA - 4 Watt Fiber Amplifier, mFALC - Mixed Fast Analog Linewidth Control, SAS - Saturated Absorption Spectroscopy, $\lambda/4$ - Quarter Wave Plate, MCP - Multi-Channel Plate.

We will begin with a discussion of the laser system, including frequency control and stabilization, before moving to the electro-optic control and amplification of the light.

5.1 DL 100 Lasers

The current generation of this experiment received a major laser upgrade from previous generations of the experiment, mostly facilitated by T. Inaki [66].This primarily consisted of the purchase of three DL 100 laser systems from Toptica Photonics, Inc.

The upgrade sought to increase the coherence of the two ARP light beams by correlating the optical phase of the two originating lasers. This can be done with a phase lock, the term for stabilizing the phase and frequency of the beat note generated by the frequency difference of two lasers. This is an incredibly delicate goal to achieve and is the reason for the major upgrade. We will discuss this in further detail in 5.1.3.

5.1.1 Laser Cavity

The DL 100 laser cavity (Fig. 5.2) begins with a Fabry-Perot laser diode, followed by a lens to collimate the beam. The beam is incident on a diffraction grating such that the first order reflection returns to the diode, providing wavelength selective, optical feedback. This feedback establishes the extended cavity, with the zeroth order reflection serving as the output.

We have 4 methods of frequency control in this cavity design. The first is the diode temperature, which regulates the size of the diode itself. The Toptica temperature controller (DTC 110) stabilizes the diode against thermal changes. Second is diode current. This controls both power and wavelength, so minimal changes are best to avoid large power fluctuations. Finally, the angle of the diffraction grating has both a coarse manual control via a screw and fine electronic control via a piezo-electric transducer (PZT).

The Toptica current controller (DCC 110) and PZT controller (SC 110) are connected via a system Toptica refers to as "feed forward", wherein the PZT controller will also control

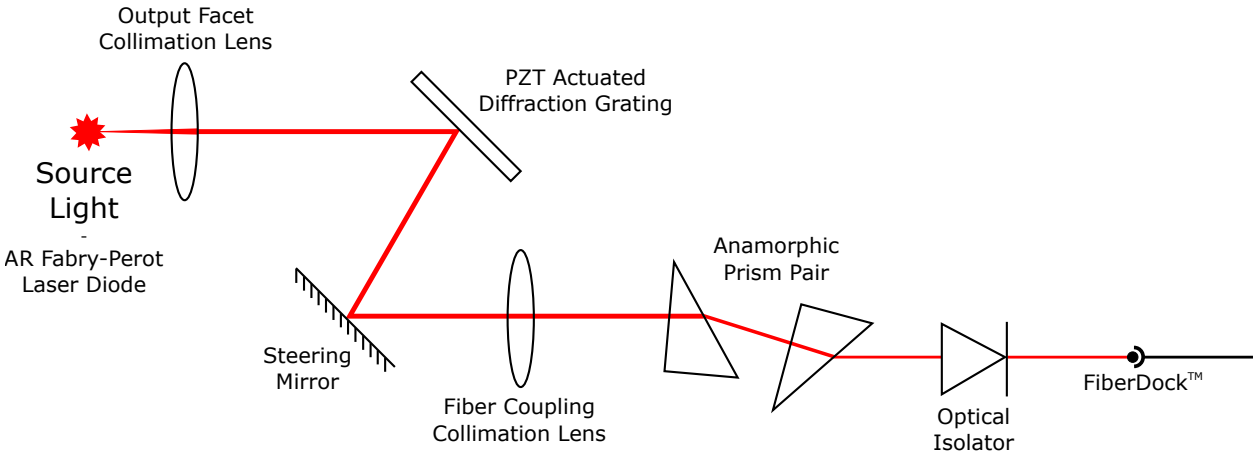

Figure 5.2: Extended cavity and optical setup for the Toptica DL 100 lasers used in our experiments. The extended cavity is in Littrow configuration.

the diode current during a PZT scan to maximize the mode hop free tuning range.

After exiting the extended cavity, the beam is redirected via a steering mirror, before being incident on a lens and a pair of anamorphic prisms to shape the beam for optimal fiber coupling. This is followed by an optical isolator to prevent unwanted feedback into the cavity. And finally, the beam is enters an optical fiber via a Toptica FiberDock$^{\text{TM}}$.

In our experiment, we are primarily using PANDA type polarization maintaining fiber. The FiberDock is oriented such that the polarization of the light entering the fiber is aligned to the slow axis of the polarization maintaining fiber.

5.1.2 Master Laser Frequency Locking

The frequency of the master laser needs to match the atomic resonance frequency. To stabilize the laser frequency from both short term fluctuations and long term drifts, we employ a common technique known as saturation absorption spectroscopy (SAS) locking, shown in Fig. 5.3.

By counter-propagating a pump and probe beam in a helium discharge cell, the Doppler-

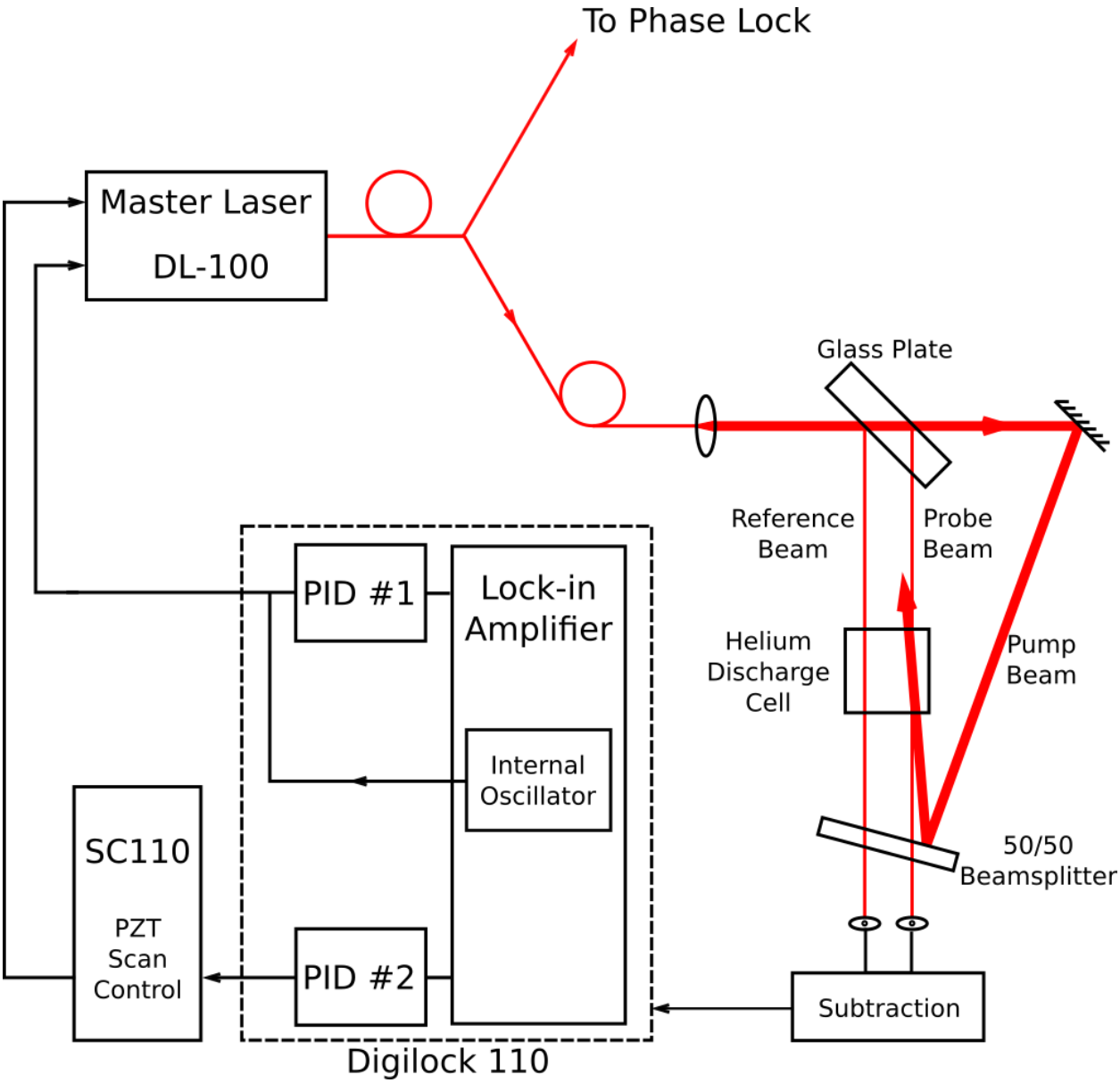

Figure 5.3: Saturated absorption spectroscopy setup for the Toptica DL 100 master laser. The Digilock 110 has two internal PID's to provide feedback on both modulation current and PZT voltage.

broadened spectrum will have narrow dips in the absorption profile of the probe beam. We can subtract this profile from an unaltered Doppler-broadened spectrum (given by the reference beam) to isolate a Doppler-free atomic spectrum.

We can feed this signal into a Toptica DigiLock 110. The DigiLock has an internal lock-in amplifier and two proportional–integral–derivative (PID) controllers. The lock-in amplifier's internal oscillator directly modulates the laser diode current (usually $\sim$7 kHz) to create a dither. With this dither, the lock-in amplifier is able to generate an error signal from the subtracted spectra.

The error signal is then fed to the two PID controllers. PID #1 controls feedback to the modulation current of the laser diode. This controller has an optional low frequency cut-off (usually 100 Hz), below which the integrator is limited.

PID #2 controls feedback to the SC 110, thereby controlling the angle of the diffraction grating via PZT voltage. It has an internal low pass filter set to match the low frequency cut-off of PID #1. This allows the two PID controllers to work together without interfering with each other; PID #1 corrects for high frequency fluctuations and PID #2 corrects for low frequency drifts.

5.1.3 Slave Laser Phase Locking

Previous ARP experiments done in our lab used two similar, independent lasers, each locked to atomic resonance. During the course of those experiments, questions arose about whether the coherence of the two light fields had an impact on the force [33, 66, 67]. To investigate this, we have implemented what is known as a phase lock to impart a shared coherence onto two lasers.

We talk about this coherence in terms of a master laser and a slave laser. The master

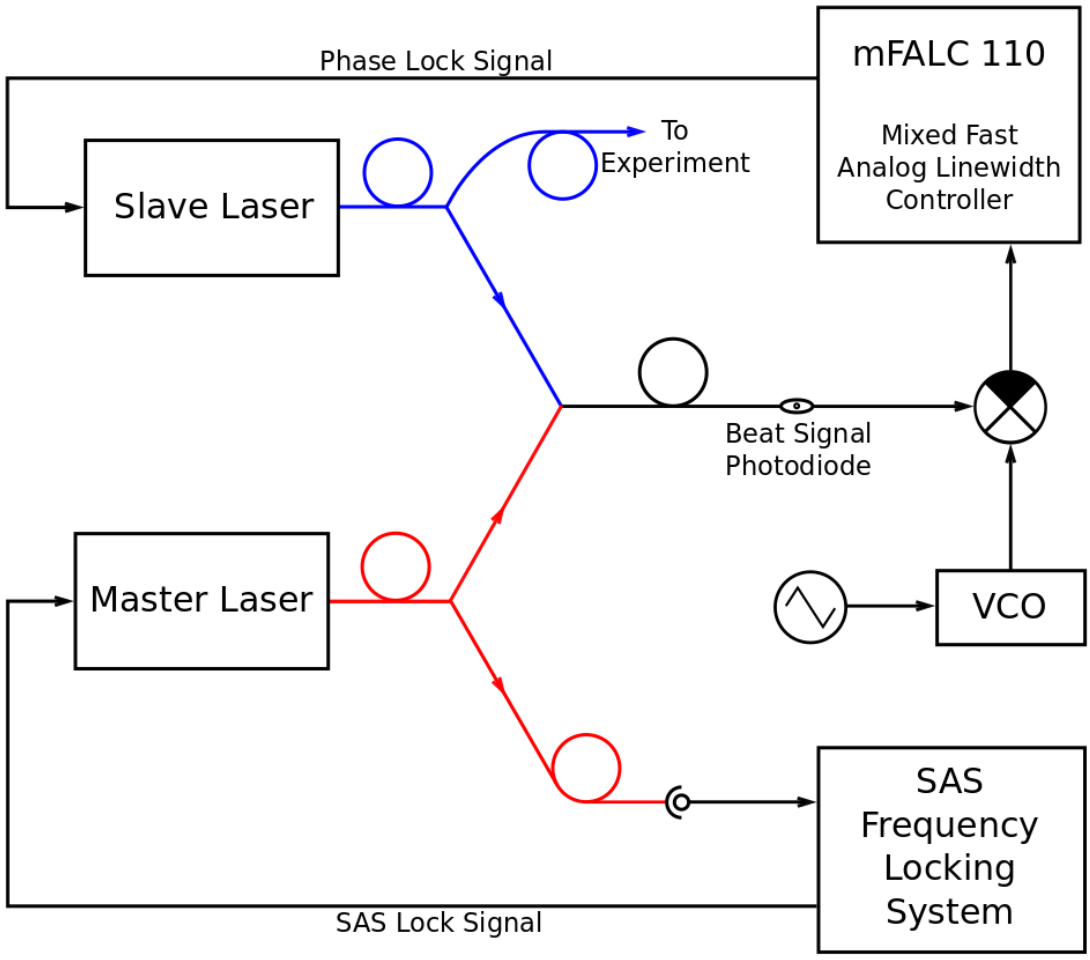

Figure 5.4: Block diagram of the phase lock setup. The master and slave laser beams are overlapped onto a photodiode to create a beat note. The phase and frequency of this beat note is stabilized to match a local oscillator signal by feedback on the slave laser. Note, only one slave laser shown; the setup is identical for both slave lasers.

laser's frequency is normally stabilized to the atomic transition frequency but it can be allowed to free-run. We look to establish feedback onto a slave laser in order that there is a stable frequency and phase difference between two lasers.

In our experiment, we have one master laser, frequency locked to atomic resonance, and two slave lasers, both phase locked to the master laser. All three of the lasers are Toptica DL-100's, so we have the freedom to exchange which lasers are assigned to master and slave, but we refrain from doing so because the settings are delicately tuned for each laser.

The two sets of phase lock equipment were bought to be identical so I will only discuss one system as pictured in Fig. 5.4. Both master and slave lasers are fiber coupled to pigtailed fiber splitters. These allow for splitting the light beams into multiple fibers or even combining two beams into one fiber. We use a second set of fiber splitters to combine a portion of the master laser's beam and a portion of the slave laser's beam into the same fiber.

These overlapped light beams will create a beat note at the frequency difference of the two lasers which can be seen by a fast photodiode. We mix this signal with that of a local oscillator (LO) in a Toptica Mixed Fast Analog Linewidth Controller (mFALC). The LO can take the form of signal generator or voltage controlled oscillator (VCO)

The mFALC provides feedback to the slave laser diode's current. This feedback will control the phase and frequency of the slave laser to meet two conditions. First, the frequency of the beat note will be stabilized to the frequency of the LO. Second, there will be a fixed phase relationship between the beat note and the local oscillator.

To meet both of these conditions requires not only a fixed frequency difference between the two lasers, but also a fixed phase relationship between the two lasers. This fixed phase relationship is what grants a shared coherence between the two lasers.

The mFALC is specified to have an optimal frequency range of 10-200 MHz. In the laboratory, we have been able to achieve phase locks with a beat note and LO frequency

range of 1-350 MHz. For phase locks with a beat note larger than 300 MHz, we use an additional set of mixers and a second LO to provide an effective beat note within the optimal 10-200 MHz range of the mFALC.

The helium discharge cell produces a large source of RF noise at 51.4 MHz which is broadcast throughout the lab. We are able to achieve a phase lock with LO frequencies $\leq$51.0 MHz and $\geq$52.0 MHz, but no closer. Additionally, there are multiple 10 MHz clock signals from various pieces of RF equipment in the laboratory. It does not prevent a phase lock at 10 MHz, but can sometimes require additional effort that is not needed for locking at nearby frequencies.

5.2 Electro-optic Modulators

In the previous sections, we discussed laser generation and frequency control of CW light. The ARP force requires pulsed light with a controlled chirp. Over the next few sections, I will discuss the electro-optical effect and how we use it to achieve this.

The electro-optical effect describes the change of the index of refraction of a material in response to the change of an external electric field. This effect can be observed in a wide variety of materials, but our experiment takes advantage of $LiNbO_3$ in the form of two types of modulators purchased from Photline Technologies. Both types consist of an integrated $LiNbO_3$ waveguide with PM fiber pigtails (see Fig. 5.5).

5.2.1 Phase Modulator

The first type of electro-optic modulator used in our experiment is the phase modulator (PM). As seen in Fig. 5.5a, the PM consists of a single waveguide path between two electrodes, one of which is connected to ground. The other electrode is connected to an RF

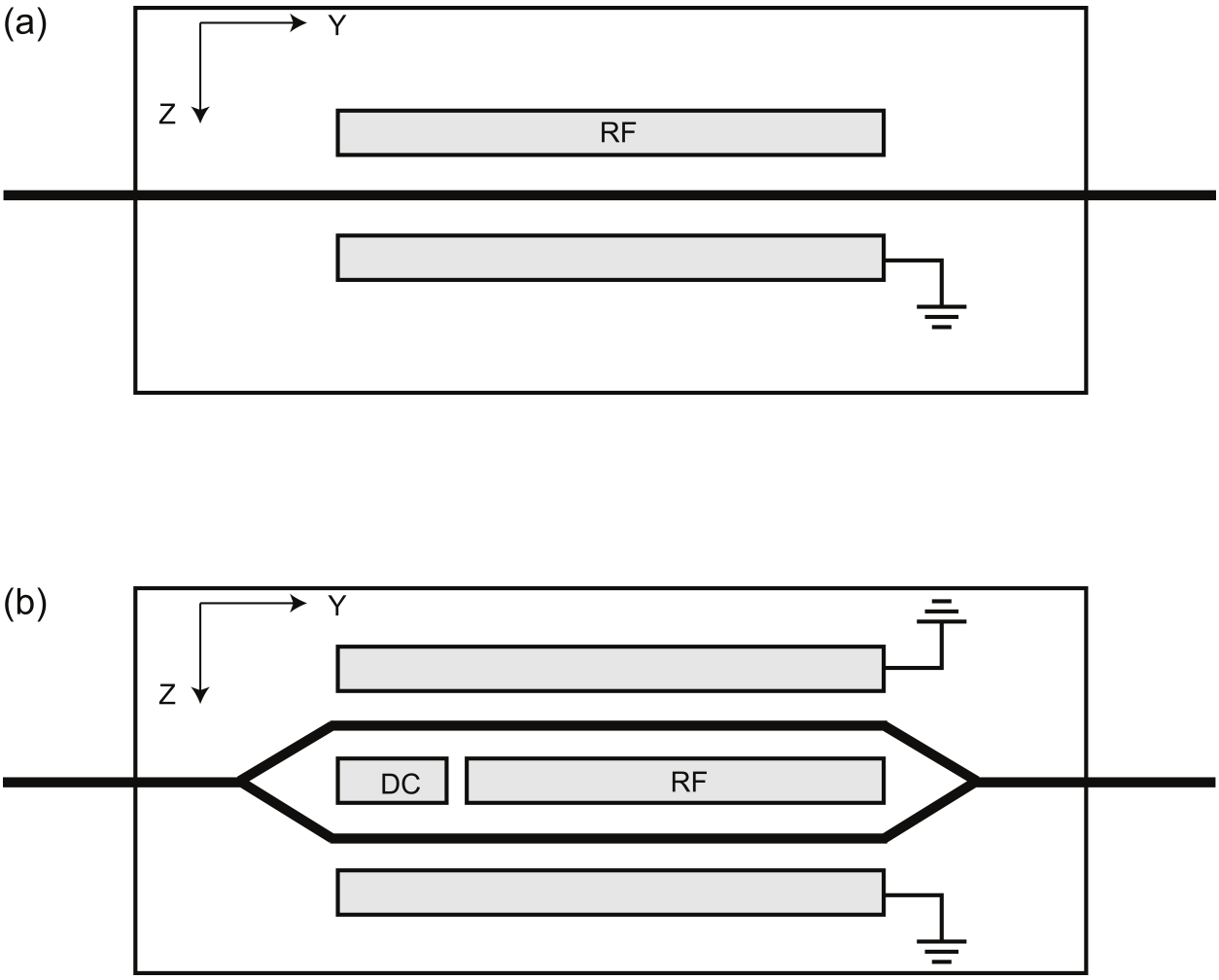

Figure 5.5: Schematic of the two types of $LiNbO_3$ modulators from Photline Technologies used in the ARP experiments. (a) The NIR-MPX-LN03 phase modulator. (b) The NIR-PX-LN03 amplitude modulator.

signal generator providing a sinosoidal voltage. For our experiments, the frequency of this signal corresponds to $\omega_m/2\pi$ =160 MHz.

The phase shift of the light passing through the PM is proportional to the strength of the electric field [68]. Since we are using a time dependent voltage, we can describe the time dependent phase of the light as

$$\phi(t) = \kappa M(\omega_m) V(t), \tag{5.1}$$

with

$$\kappa = \frac{\pi}{\lambda G} n_e^3 r_{33} \eta L. \tag{5.2}$$

L is the length of the electrodes and G is the gap between the electrodes. r_{33} is the electro-optic coefficient. n_e is the index of refraction for light polarized along the extraordinary axis. Together, this makes κ constant for a given device. The dimensionless parameter $M(\omega_m)$ describes the frequency dependence of the phase delay.

One of the more useful means of describing a PM is the voltage required to achieve a phase shift of π, known as V_π. By combining Eqn. 5.1 and 5.2, we can find

$$V_\pi(\omega_m) = \frac{\lambda G}{n_e^3 r_{33} \eta L M(\omega_m)}. \tag{5.3}$$

Although this can be directly calculated, it is often much easier to measure.

In our experiments, we apply a sinusoidal voltage to the PM. For an amplitude of V_o, the optical field can be described as

$$E(t) = E_o \cos(\omega_\ell t - \beta \sin(\omega_m t)) \tag{5.4}$$

where

$$\beta = \frac{\pi V_o}{V_\pi(\omega_m)}. \tag{5.5}$$

The time derivative of the total phase gives the instantaneous frequency

$$\omega(t) = \frac{d\phi(t)}{dt} = \omega_\ell - \beta\omega_m \cos(\omega_m t). \tag{5.6}$$

5.2.2 Amplitude Modulator

The second type of electro-optic modulator used in our experiment is the amplitude modulator (AM). As seen in Fig. 5.5b, the AM consists of a waveguide path that splits and reconnects as a Mach-Zehnder interferometer. Outside of the two paths are electrodes connected to ground. Between the two paths are two electrodes, one connected to a DC supply, the other connected to a Tektronix DTG5274 Data Timing Generator providing periodic pulses.

The interferometer design allows control of constructive and destructive interference at the recombination point to determine the output light intensity. The design of the electrodes allows for the opposite phase shift, $\pm\phi(t)$, of each arm. This allows the electric field at the recombination point to be written

$$E(t) = \frac{E_o}{2}[\sin(\omega_\ell t + \phi(t)) + \sin(\omega_\ell t - \phi(t))] = E_o \sin(\phi(t)) \sin(\omega_\ell t). \tag{5.7}$$

The resulting field contains amplitude modulation but no phase modulation.

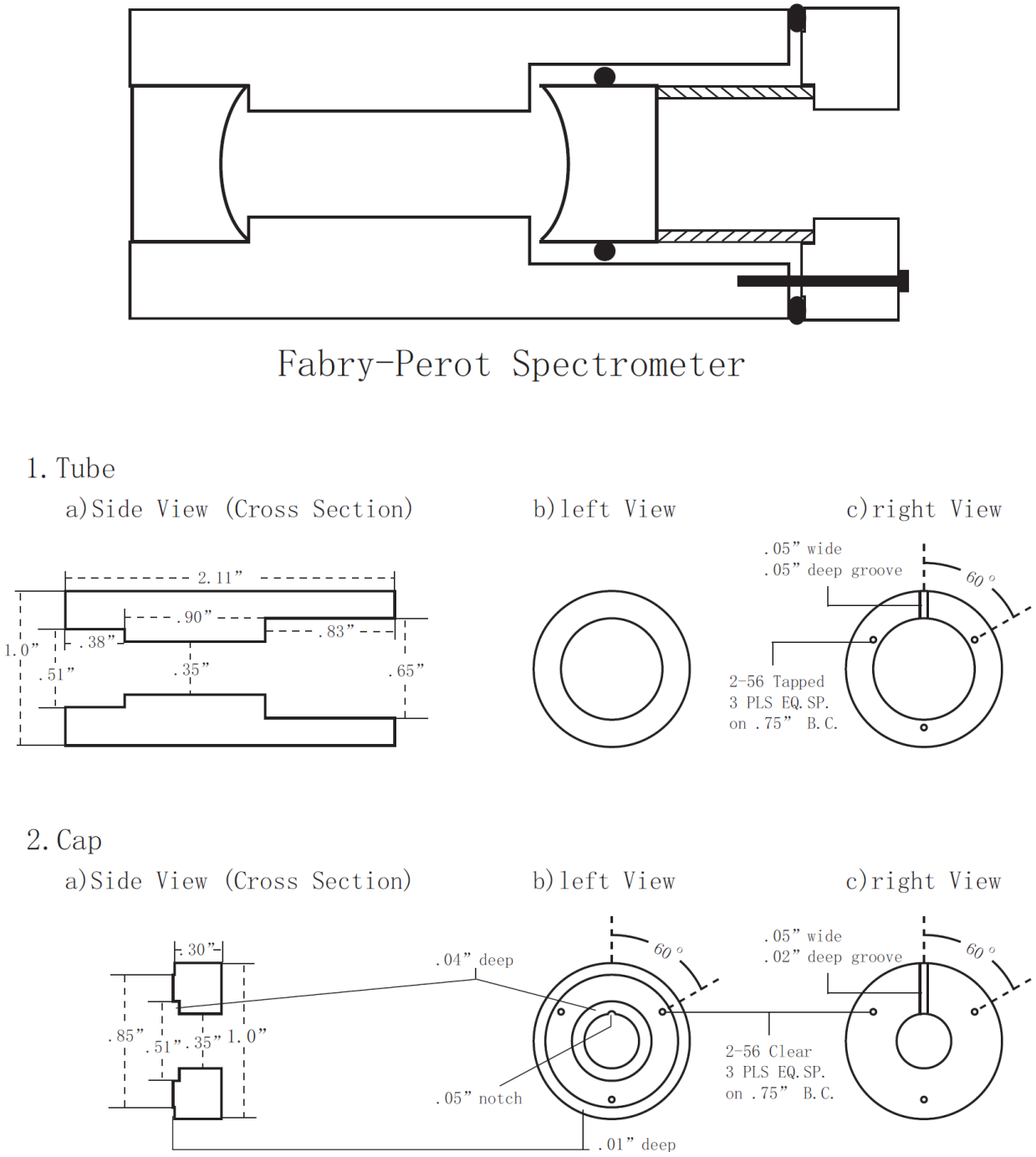

Figure 5.6: Schematic of the home-built scanning Fabry-Perot interferometer. The mirror focal length and cavity length are both 25 mm. The free spectral range is ≈3 GHz with a resolution of ∼30 MHz. From [43].

5.2.3 Pulse Characterization

As discussed in Chap. 3, our experiments require half sine pulses at 25% duty cycle under a cosinusoidal chirp. In our experiment, the light passes through the PM to receive the chirp before entering the AM to become a train of pulses. In our discussion, we will cover this in reverse, beginning with the intensity modulation before returning to the frequency modulation.

To create the pulses, the DTG5274 operates at 320 MHz with 1/4 pulse rate and 17% duty cycle. This outputs a nearly triangle pulse with a base width of ∼3.125 ns and a repetition rate of 80 MHz. We use a Thorlabs DET08CFC 5 GHz fast photodiode to monitor the light's intensity profile and a home-built, scanning Fabry-Perot (FP) interferometer (see Fig. 5.6) to monitor the frequency spectrum. We tune the DC voltage for destructive interference between pulses. An example of an ideal pulse train's intensity profile and frequency spectrum can be seen in Fig. 5.7 and 5.8, respectively.

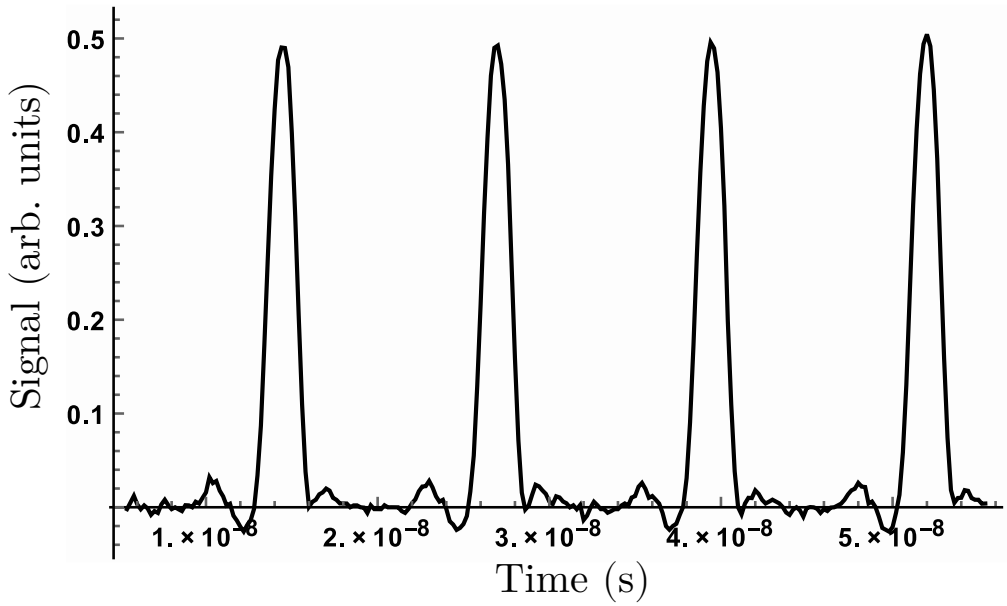

Figure 5.7: An intensity profile of good optical pulses as measured by a Thorlabs DET08CFC 5 GHz fast photodiode.

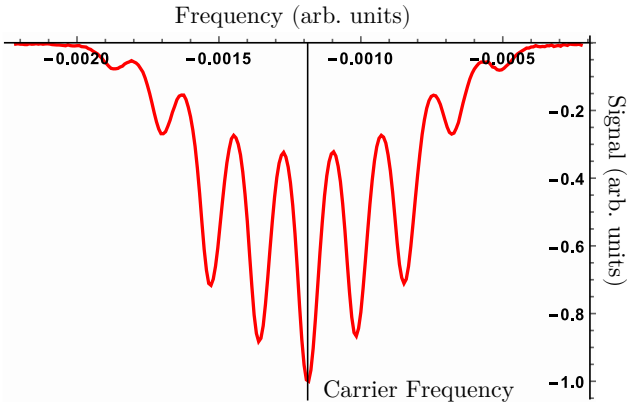

Figure 5.8: Frequency spectrum of a train of properly shaped pulses. Peaks are separated by the 80 MHz repetition rate and extend to the 320 MHz bandwidth. Measured using a home-built, scanning Fabry-Perot interferometer pictured in Fig. 5.6.

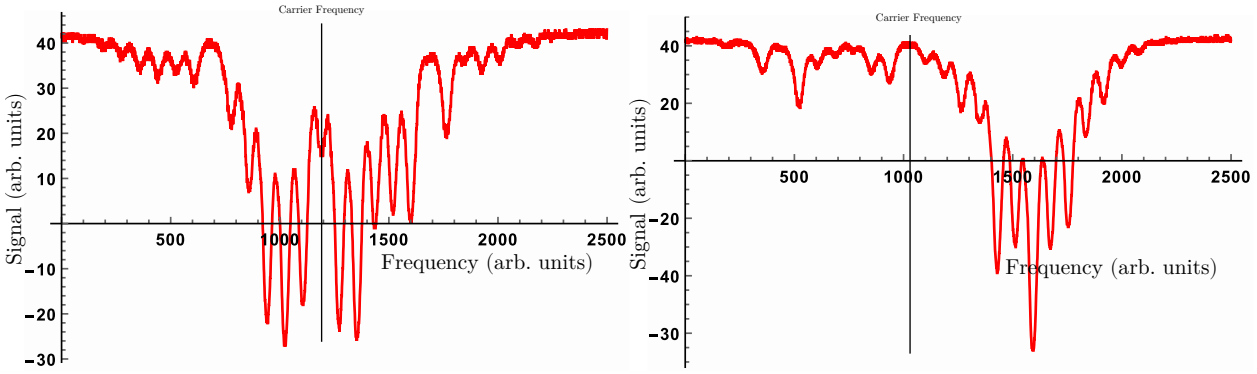

(a) Properly Aligned Chirped Pulses (b) Misaligned Chirped Pulses

Figure 5.9: Comparison of the frequency spectrum of chirped pulses with and without proper alignment in time. Peaks are a combination of the 80 MHz repetition rate with 320 MHz bandwidth of the pulses and 160 MHz repetition rate with tune-able bandwidth of the chirp. Measured using a home-built, scanning Fabry-Perot interferometer pictured in Fig. 5.6.

Once the pulse shape is set, we can set a relative delay between the two electronic pulses. The DTG5274 allows for the tuning of the relative delay in increments as small as 0.2 ps. We also use an RF trombone for manual tuning of the delay. By tuning the delay of the electronic pulses, we also tune the delay of the resulting optical pulses.

After the pulse shape and timing are tuned properly, we turn on the phase modulation.

The chirp consists of half of a cosine wave sweeping symmetrically through ω_ℓ at the modulation frequency $\omega_m = 2\pi \times 160$ MHz $\sim 100\gamma$. To ensure a symmetric sweep, we tune the phase of the sweep while monitoring the frequency spectrum on the FP, as seen in Fig. 5.9. The signal generators can be tuned digitally in 1deg increments. The 80 MHz pulse repetition rate is commensurate with the 160 MHz modulation frequency. Therefore, once set, the relative phase of the pulse and chirp will be constant because we use the 10 MHz clock signal of the DTG5274 as the reference clock for both of the signal generators that power the PM's.

5.3 Amplifiers

As we saw in Eqn. 1.3, $\Omega(t) \propto |\overrightarrow{E}(t)| \propto |\sqrt{I(t)}|$. Typical experiments require power on the order of $\sim$1 W. In order to achieve the high intensities required, we rely on the aid of two types of optical amplifiers.

5.3.1 Booster Optical Amplifiers

First, we rely on the aid of semiconductor (GaAs) based amplifiers. Our experiment uses pair of Thorlabs BOA1137P booster optical amplifiers (BOA) to provide small signal gain. It is described as a semiconductor diode laser with anti-reflective coatings instead of highly-reflective coatings on its faces to prevent feedback and therefore the necessary cavity to produce lasing.

BOA's are able to provide the small signal gain we need, but can have their drawbacks. Pulsed light through a BOA will red-shift the light in a process called self-phase modulation [69]. Therefore, we must use the BOA's before the AM's.

5.3.2 Fiber Amplifiers

The BOA's provide a small signal gain, but to get to the ∼1 W we require, we rely on a pair of Keopsys KPS-BT2-YFA 4 W fiber amplifiers (4WFA). The fiber amplifiers use Yb-doped fibers as a gain medium. They absorb the 980 nm diode pump light and emit light from 1050 - 1100 nm. Seed light is amplified by spontaneous emission and the gain is proportional to the power of the 980 nm pump light.

5.4 Optical Transport

Now that we have covered the optical devices of our system, we shift the discussion to the overall optical path. Returning to Fig. 5.1, master and slave lasers are all coupled to the slow axis of PANDA PM980 type polarization maintaining (PM) fibers.

In order to split the light between beams intended for experiment and for locking, we use PM fiber fused couplers FUSED-22-1064-6/125-XX/YY-3A3A3A3A-1-1-PM from Oz Optics, where the XX/YY stands in for the approximate splitting ratio (ex. 90/10 or 50/50). Each of the fiber coupled components (PM, BOA, AM, and 4WFA) are PM coupled and rely on input light along the slow axis.

After exiting the 4WFA, the light passes through a fiber output coupler to return to a free space beam. We use a $\lambda/2$ plate and polarizing beam-splitter cube (PBC) to pick off a small percentage of the beam to send to the FP and fast photo-diode for the analysis described in Sec. 5.2.3.

The primary beam travels through the PBC to the beam shaping optics. We use a spherical telescope and a cylindrical telescope to expand the beam to 6.0 mm by 2.0 mm. The light passes through an adjustable slit followed by a 4F imaging system to produce an image of the slit at the approximate point of the interaction region.

The adjustable slit only collimates the beam in the long dimension. We do this to mimic a flat-top intensity profile for the atomic beam (which travels transverse to the light field). By tuning the width of the slit, we are able to control the distance over which the atoms are in the light field. As mentioned in Sec. 4.2, the atoms have an average velocity of ~ 1000 m/s. A slit width of 3.75 mm provides the atoms with an average of 3.75 μs = 300 pulse pairs.

Finally, before entering the vacuum system, the light beams pass through a $\lambda/4$ plate to make the polarization circular. This allows for the ARP beams to take advantage of optical pumping to ensure all atoms will experience the same Rabi frequency, as seen in Fig. 4.3. To improve this effect, we can utilize an optical pumping stage upstream of the experiment.

The optical pumping beam is a resonant light beam taken from the master laser. We use a cylindrical telescope to shape the beam into a 1.0 mm by 3.0 mm beam. It travels very nearly parallel to the ARP beams through the same $\lambda/4$ plate. It enters the vacuum system and crosses the atomic beam a variable distance (usually ~ 5 mm) upstream of the ARP beams (Fig. 5.1), both within the Helmholtz coils. The atomic beam traverses the shorter dimension of the optical pumping beam. This allows for an interaction time of ~ 1 μs, or ~ 5 cycles. As mentioned in Sec. 4.1, this ensures that $\sim 97\%$ of the atoms will be in the $m_j = +1$ ground state prior to encountering the ARP beams.

5.5 Alignment Procedure

Over the course of this chapter, we have outlined a large number of components. Each day, in order to run the experiment, we must follow a specific procedure to incorporate all of these components.

1. Align the resonant optical pumping beam to optimize for the strongest push with

limited power (usually ~ 5 mW).

2. Align resonant ARP beam coming from the same side as the optical pumping beam, to optimize for the strongest push with limited power ($\lesssim 50$ mW).

    - This can be done with pulses either on or off but the chirp must be off.
    - These two beams will be very close to parallel, but perfectly parallel is not ideal.

3. Align the counterpropagating second ARP beam onto the first ARP beam.

    - Horizontal alignment is most important; vertical will be readjusted later.

4. Bring both lasers close to resonance, turn on pulses, and match beam powers (> 300 mW).

    - Both lasers locked to resonance is ideal but not currently possible without buying or borrowing equipment.
    - The minimum power ensures that the peak intensity exceeds the minimum to produce a pi-pulse.

5. Align the vertical angle of the second ARP beam to provide a symmetric force profile.

6. Adjust the relative pulse timing electronically using the DTG5274 and/or manually using the RF trombone to to optimize for the strongest push.

    - Usually the strongest force occurs symmetrically in the wings rather than the center.
    - Both the laser frequency and optical pulse shape can drift on the same timescales as the adjustment process; readjust as necessary.

- Adjustments to the pulse timing can reveal errors in the vertical alignment; repeat the previous step as needed.

7. Align chirp timing onto the optical pulses for a symmetric frequency sweep either up or down.

Once alignment is complete, set laser powers, detunings, and chirp ranges as desired to begin data collection.

Chapter 6

Measurement of Optical Forces

In order to better understand the usefulness of the ARP force, we have conducted experiments to measure the magnitude of the force across a wide velocity range (∼hundreds of m/s). We will begin with a brief exploration of optimal values for Rabi frequency and chirp range (Sec. 6.1). Then we will focus on the velocity dependence of the force (Sec. 6.2) for carefully selected parameters. Finally we will explore the evolution of optimal values for Rabi frequency and chirp range as a function of velocity (Sec. 6.3).

6.1 Initial ARP Force Parameters

As we saw in Sec. 3.3, optimization of the ARP force requires a delicate balance of chirp range and Rabi frequency. To better determine candidates for optimal parameters, we take images of the ARP force deflection for a range of chirp and Rabi frequency settings. We fit to each image (see Fig. 4.7 for an example) in order to determine the deflection and hence the strength of the force for each image. These force values from the fits are plotted against the chirp range and the Rabi frequency. We call the resulting plot a forcemap and can be

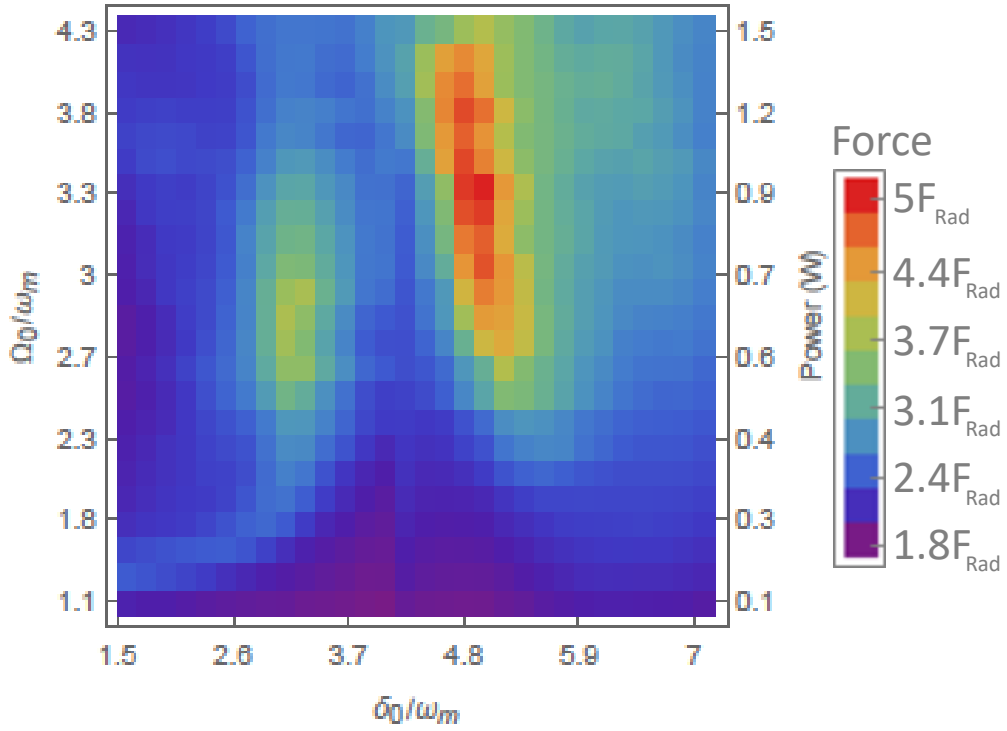

(a) Experiment, ∼300 pulse pairs

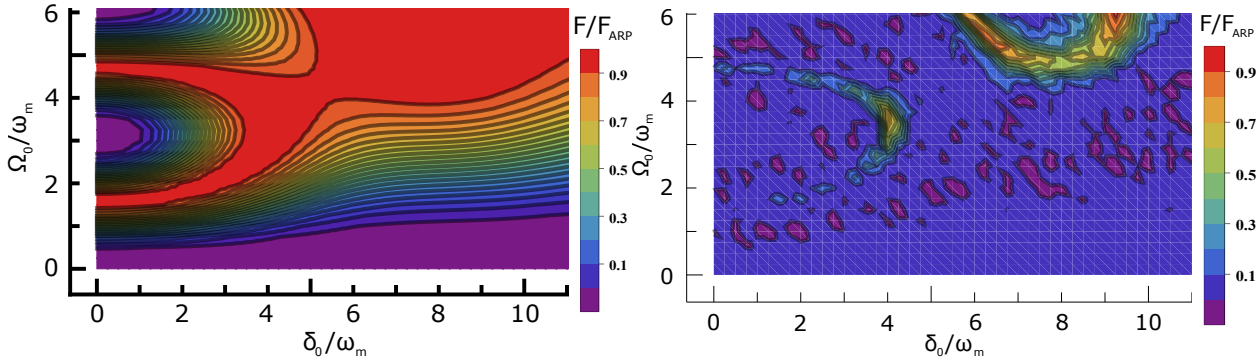

(b) Simulation, 1 pulse pair.

(c) Simulation, 320 pulse pairs.

Figure 6.1: To better determine ideal parameters for the ARP force, we measure the strength of the force over a large grid of values for peak Rabi frequency, Ω_0, and chirp range, δ_0. Each pixel is one measurement. The regions of strongest force are red and the regions of weakest force are purple. The regions of strong forces near $\Omega_0/\omega_m = 2.9$, $\delta_0/\omega_m = 3.1$ and $\Omega_0/\omega_m = 3.4$, $\delta_0/\omega_m = 4.9$ will be referred to as region 1 and region 2, respectively. Parts (b) and (c) show a limited range of the numerical simulations Fig. 3.6 for easier comparison. The maximum force shown in the simulations, $F = F_{ARP} \approx 19F_{Rad}$.

seen in Fig. 6.1a. Included as parts b and c are a small region of the numerical simulation forcemaps shown earlier in Fig. 3.6.

There are two regions of strong optical forces in Fig. 6.1a. We will refer to the parameter set near $\Omega_0/\omega_m = 2.9$, $\delta_0/\omega_m = 3.1$ as region 1 and $\Omega_0/\omega_m = 3.4$, $\delta_0/\omega_m = 4.9$ as region 2.

The laser upgrades mentioned in Sec. 5.1 allowed for a larger scan of both chirp range and Rabi frequency than those of previous iterations of our experiment, such as those seen in Ref. [43]. These previous experiments were able to observe region 1, but not region 2.

As stated earlier, Fig. 6.1a is a small region of the forcemaps shown earlier in Fig. 3.6. Modified versions of Fig. 3.6 are placed as Fig. 6.1b and c for easier comparison. The crescent shape of region 1 closely mimics what we see in Fig. 6.1b and c but occurs for a lower chirp range.

With the accessibility of the larger chirp range and Rabi frequency, we expect to encounter a second crescent shape, tilted sharply clockwise from the first crescent. Region 2 appears in an area we do not expect to observe a large force. It may be related to the second expected crescent, but it occurs for lower values of both Rabi frequency and chirp range. Also, we only see a line of strong forces, not a crescent. It is not yet clear as to whether or not Region 2 and the second expected crescent are related.

To further study this phenomenon, future experiments must further expand the experimentally accessible parameters.

6.2 Force *vs.* Velocity

When discussing an optical force, we are not simply interested in the maximum force that can be produced. We also need to understand the velocity dependence of the force. This may reveal how suited a particular force may be for different applications, such as slowing

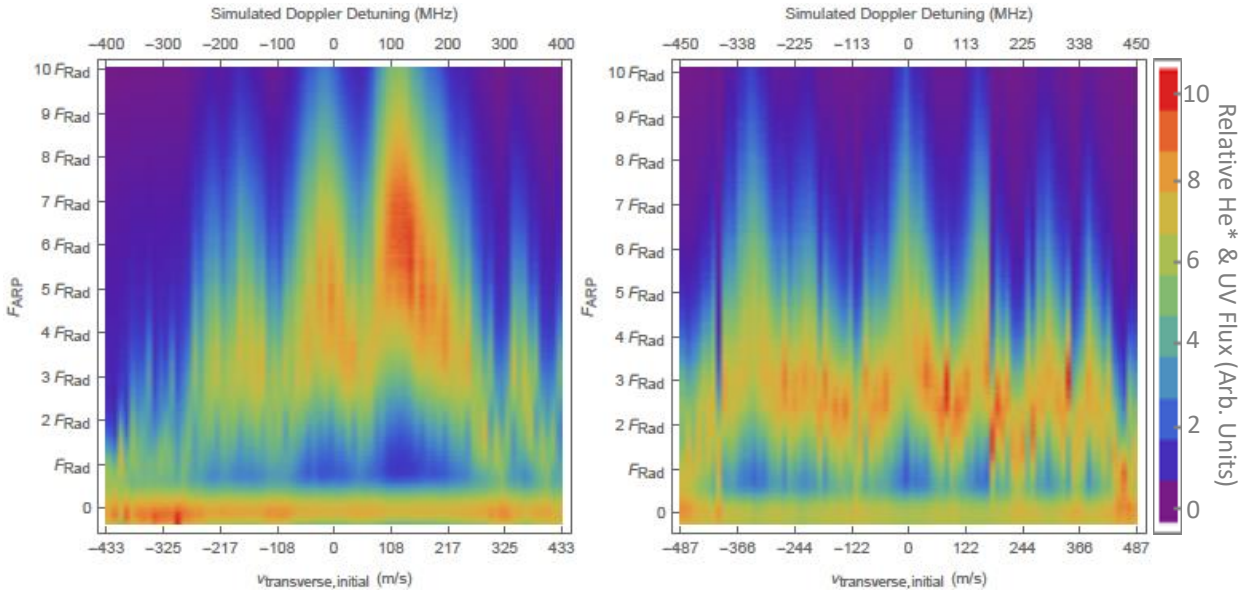

(a) $\delta_0/\omega_m = 2.85$, $\Omega_0/\omega_m = 3.05$ (b) $\delta_0/\omega_m = 3.35$, $\Omega_0/\omega_m = 4.94$

Figure 6.2: Force vs. velocity for $\Omega_0/\omega_m = 2.85$, $\delta_0/\omega_m = 3.05$ (region 1) and $\Omega_0/\omega_m = 3.35$, $\delta_0/\omega_m = 4.94$ (region 2). Each vertical column of pixels represents line-outs taken for a particular simulated transverse velocity. The background of the source passing through the slit can be seen at the bottom of the image.

or cooling.

As described earlier, we can oppositely detune the counter-propagating transverse laser beams to simulate the Doppler shift of an atom moving transverse to the atomic beam axis (i.e., along the light beams). We can use this to explore the velocity dependence of the force.

As described in Sec. 4.3 and seen in Fig. 4.7, the atoms are deflected horizontally away from the UV background image left by the source and slit. We rotate the image to present this as a vertical deflection. We can take a series of images and use each vertical spatial distribution as an individual column as in Fig. 6.2. We should also note that atoms with the same transverse velocity (as a result of the ARP force) will hit the detector at a different place depending on their longitudinal velocity and this is what provides the spread in the vertical column.

In Fig. 6.2, we present the measurements of the ARP force for a series of simulated velocities. Fig. 6.2a corresponds to region 1 and Fig. 6.2b corresponds to region 2. In both images, the x-axis is the simulated velocity transverse to the atomic beam axis. Each column is created using one image of the atoms undergoing the force at that particular simulated velocity.

For the experimental parameters, $\omega_m = 2\pi \times 160$ MHz $\sim 100\gamma$ and the value of dead time equal to $2\pi/\omega_m$, the theoretical maximum force is $F_{ARP,ideal} \approx 32\ F_{Rad}$ and the effect of spontaneous emission is to reduce the force to $F_{ARP,spont} \approx 19\ F_{Rad}$. We observe forces of up to 7 F_{Rad} in region 1 and up to 5 F_{Rad} in region 2, both significantly smaller than predicted.

We do also want to note the discrepancy between the measured force of Fig. 6.1 showing strongest forces in region 2, while Fig. 6.2 shows strongest forces in region 1. Fig. 6.1 was obtained using resonant light and therefore all of the measured forces correspond to atoms with an initial transverse velocity of 0 m/s. In Fig. 6.2, we see that the peak forces occur for atoms of an initial transverse velocity $\sim +125$ m/s for region 1 and ~ 0 m/s for region 2. Re-comparing the forces for atoms of ~ 0 m/s, Fig. 6.2 shows almost equal forces. This discrepancy is presently unresolved.

The velocity capture range is quite large, extending between ~ -300 m/s to $\sim +350$ m/s for region 1 and $\sim \pm 450$ m/s for region 2. Intuitively, the ~ 1.5 times larger chirp range of region 2 provides the ~ 1.5 larger velocity capture range.

Our naive view of the velocity dependence of ARP suggests that the force is maximum at $v = 0$ and tapers smoothly to zero at some v_{max}. This view is generally supported by the results of numerical calculations shown in Fig. 3.9 as well as those in Ref. [67]. But this is not at all what we see. Instead we observe large peak and valley structures of the velocity dependence.

The valleys of region 1 (Fig. 6.2a) are separated by $\sim$150, 120, and 280 MHz and its

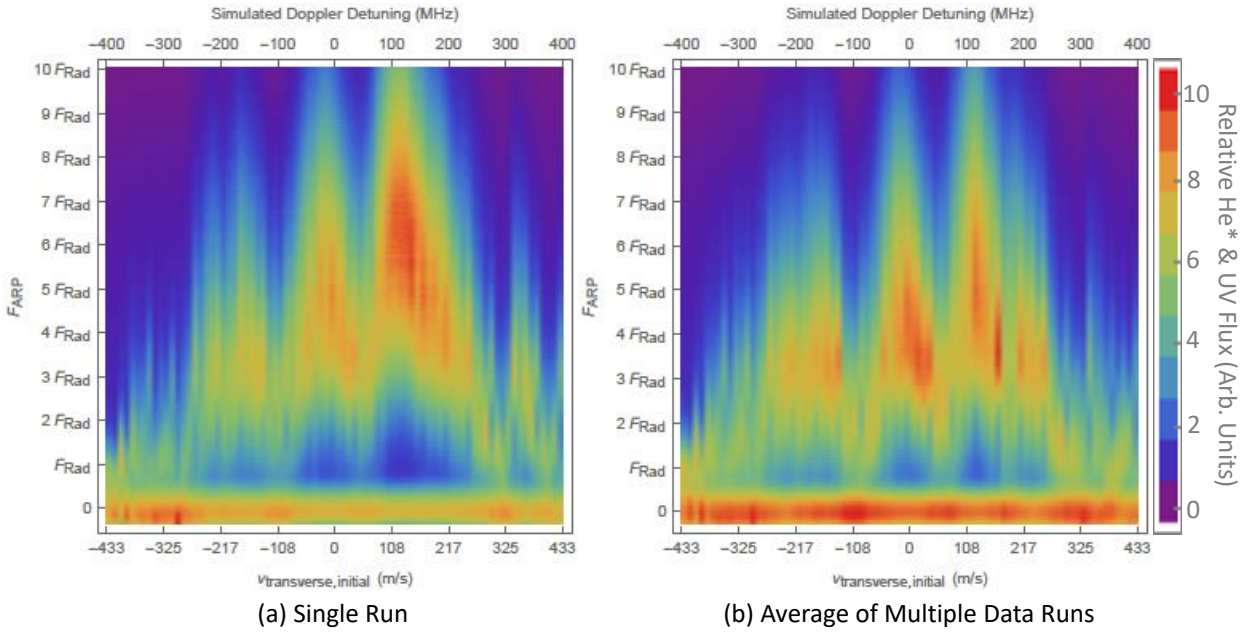

(a) Single Run (b) Average of Multiple Data Runs

Figure 6.3: Comparison of force vs. velocity for $\Omega_0/\omega_m = 2.85$, $\delta_0/\omega_m = 3.05$ (region 1) for a single data run (a) and averaged over multiple data runs (b). Fig. 6.2a is reproduced here as (a) to help the reader with the visual comparison. Each vertical column of pixels represents line-outs taken for a particular simulated transverse velocity. The background of the source passing through the slit can be seen at the bottom of the image.

peaks are separated by ∼180, 150, and 220 MHz. The valleys of region 2 (Fig. 6.2b) are separated by ∼220, 140, 200, 120, 100, and 100 MHz and its peaks are separated by ∼120, 200, 140, 120, and 80 MHz. The structures hint at a periodicity, but do not yield to a detailed analysis.

When we first observed these structures, we believed them to be a form of experimental error; i.e. some sort of accrual of systematic errors over the course of the long data acquisition time. We repeated measurements over months, varying the acquisition order, and continued to observe the structures occurring for the same simulated velocities. Averaging the data across multiple runs gave us Fig. 6.3b where the structures persist.

Next, we wanted to focus on the role of spontaneous emission. As we discussed in

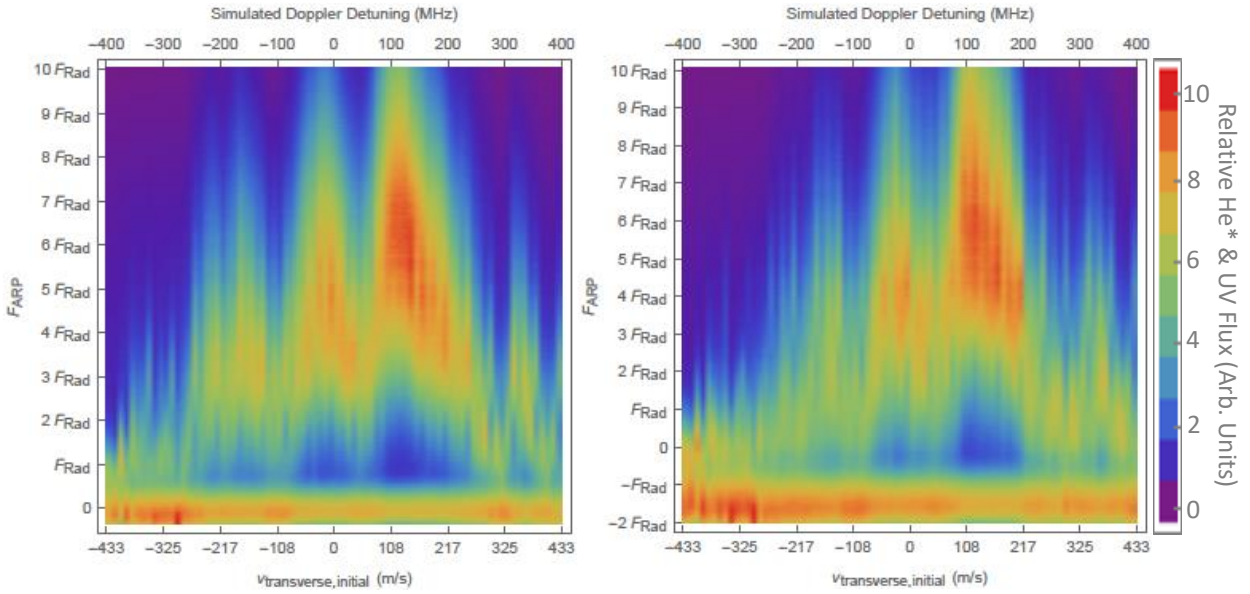

(a) 300 Pulse Pairs (b) 200 Pulse Pairs

Figure 6.4: Force vs. velocity for $\Omega_0/\omega_m = 2.85$, $\delta_0/\omega_m = 3.05$ (region 1), for 300 and 200 pulse pairs. Fig. 6.2a is reproduced here as (a) to help the reader with the visual comparison. Each vertical column of pixels represents line-outs taken for a particular simulated transverse velocity. The background of the source passing through the slit can be seen at the bottom of the image.

Sec. 3.2, as the number of pulse pairs increases, spontaneous emission will reduce the average force to $F_{ARP,spont} \approx 19F_{Rad}$. We can explore this effect by changing our interaction time. The measurements shown so far were conducted with the transverse laser beams limited by 3.75 mm slits. This provides the atoms with an average of $\sim$3.75 μs interaction time, corresponding to approximately 300 pulse pairs. By using a 2.5 mm slit, we can provide the atoms with an average of $\sim$2.5 μs interaction time, corresponding to approximately 200 pulse pairs.

As seen in Fig. 6.4, there are very minimal differences in the forces observed between the two interaction times. We appear to be past the point of distinguishability with the asymptotic limit of the force (see Fig. 3.4). Attempted measurements with interaction times

lower than 200 pulse pairs did not provide significant deflection from the source background image. In future experiments we may introduce additional beam pipe length to allow for greater transverse displacement for the smaller momentum changes of shorter interaction times.

6.3 Force Parameter Search

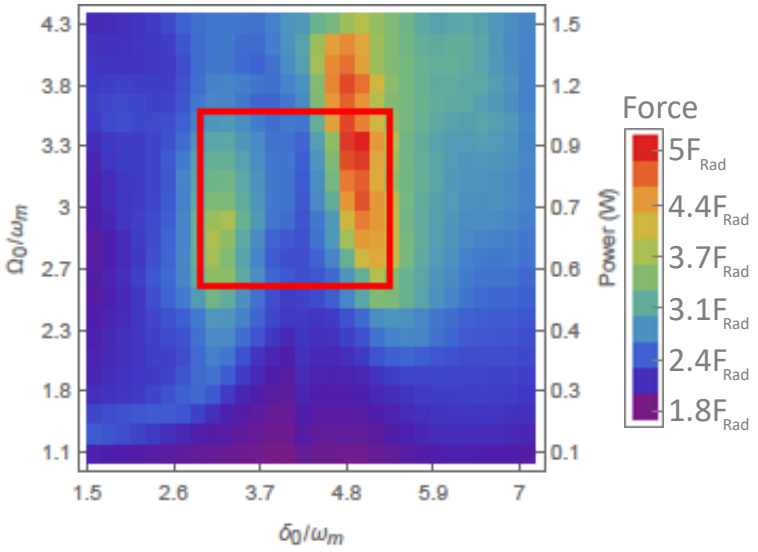

Figure 6.5: Small region of Fig. 6.1a to specify the parameter range used in other measurements. The regions of strongest force are red and the regions of weakest force are purple.

The velocity dependency measurements of Sec. 6.2 left us with many unanswered questions, in particular, the large peaks and valleys seen in Fig. 6.2. To better study this, we need to change the perspective of our measurements. Instead of selecting a particular set of parameters for Rabi frequency and chirp range to measure the velocity dependence, we can select a set of particular velocities and measure the force for a wide range of Rabi frequencies and chirp ranges at each velocity. These would be what we've previously termed as a forcemap to describe Fig. 3.6 and 6.1.

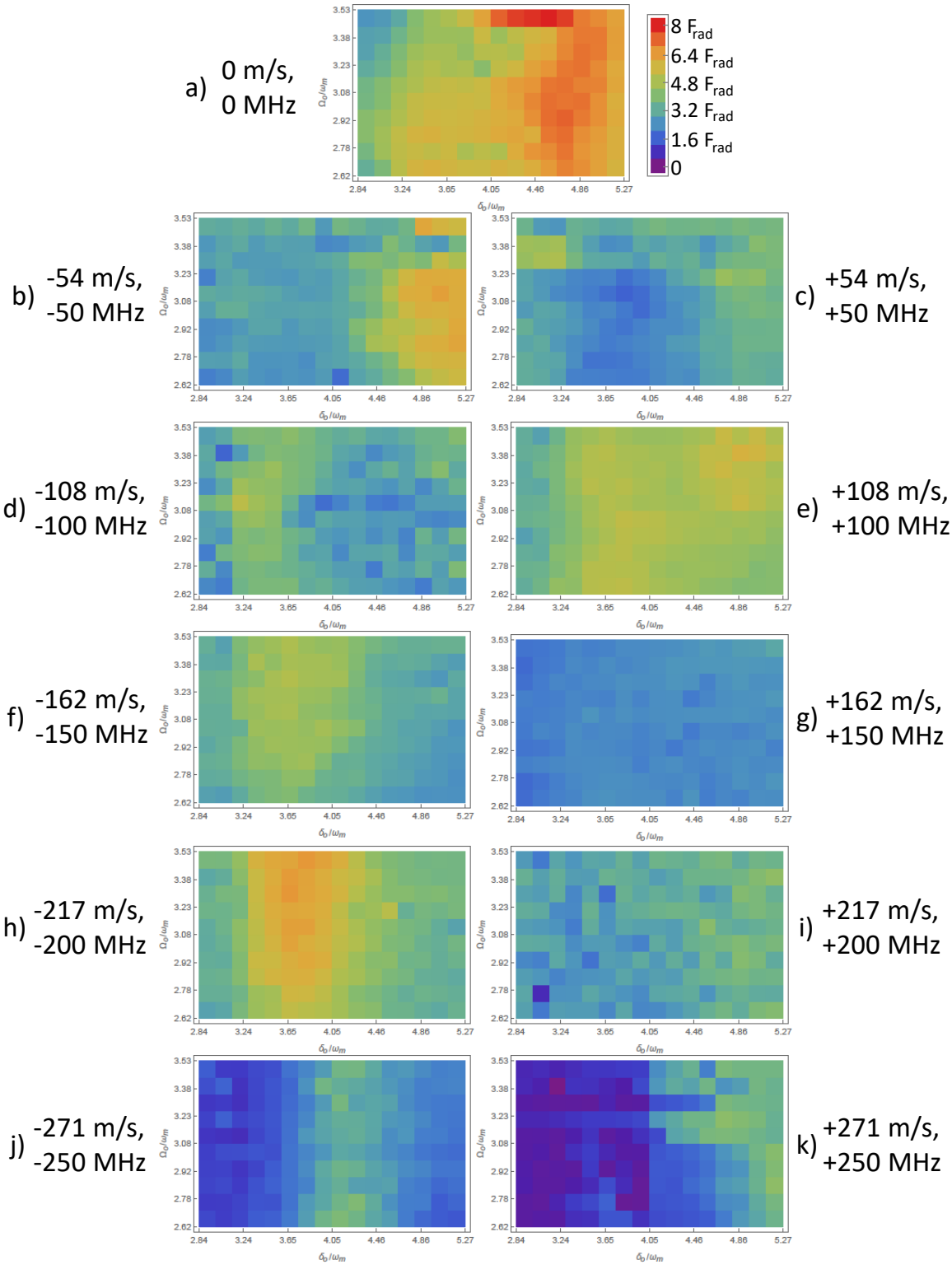

Figure 6.6: Forcemaps taken for a regular set of simulated velocities.

Because of the length of time of the measurements, we need to select a smaller range of these parameters, as shown in Fig. 6.5. This allows us to capture the velocity sensitivity at the previously measured regions 1 and 2, while also observing an array of nearby parameters.

Fig. 6.6 shows forcemaps taken for a regularly spaced set of simulated velocities, also listed by the required detunings. For each simulated speed, the positive and negative versions show stark differences.

For one explanation of this, we consider ±54 m/s. For atoms that begin at -54 m/s, positive forces will lower their speed but for atoms that begin at +54 m/s, positive forces will increase the speed. Even though ±54 m/s should have identical instantaneous forces, as they move to lower and higher speeds, respectively, their Doppler shifts diverge, allowing their instantaneous forces to evolve differently.

Given the interaction of ∼300 pulse pairs and the theoretical maximum (not including spontaneous emission) of $2\hbar k$ momentum shift per pulse pair, this would result in a total velocity change of ≈55 m/s. We are measuring average force magnitudes much smaller than this (∼ 1/4 to 1/16), but it is enough to show that the speeds (and therefore the Doppler shifts) of the two atoms in the example will diverge quickly.

We can also examine the differences between neighboring forcemaps. We would expect to be able to track the changes to each forcemap sequentially. For some of these velocities, it is easy to do, but for others, the evolution remains obscured.

Figs. 6.6d, f, h, and j feature a nearly vertical line of strong forces centered on δ_0/ω_m ≈3.3, 3.6, 3.7, and 4.1, respectively. While the strength of the forces vary, there is nearly a linear relationship between the chirp range of the peak force and the simulated Doppler detuning. This particular relationship is not seen in the other images.

It appears that there may be a different relationship between Figs. 6.6a, b, and c. This relationship is not as clear but still worth describing. Fig. 6.6a features an oddly shaped line

of strong forces centered on $\delta_0/\omega_m \approx 4.7$. Fig. 6.6b features a similarly shaped, albeit weaker, line of strong forces that appears to be centered on the edge of our scan at $\delta_0/\omega_m \approx 5.2$. Fig. 6.6c appears to similarly show the left edge of the shape but in this case, more of it appears to be off the edge of our scan range and the forces are significantly weaker. These effects obscure whether or not this is related to what we see in Figs. 6.6a and b.

Figs. 6.6e, g, and i show very limited amounts of structure. It is not clear if there is any relationship between these images. It is interesting to observe the wide area of strong forces in Fig. 6.6e, the wide area of low forces in Fig. 6.6g, and a resurgence of the force in Fig. 6.6i. This is reminiscent of the almost periodic velocity dependence seen in Sec. 6.2.

There may also be a tenuous connection between Figs. 6.6i and k. Fig. 6.6i shows slightly stronger forces for higher values of δ_0/ω_m and slightly weaker forces for lower values of δ_0/ω_m. Fig. 6.6k shows reasonable forces for higher values of δ_0/ω_m and forces around 0 for lower values of δ_0/ω_m.

To draw a greater understanding of the sensitivity to parameter selection, future experiments should aim to both expand the range of parameters being scanned as well as to study this effect in smaller velocity steps. The biggest hurdle to achieving either of these goals is to reduce the extremely long data taking process.

Chapter 7

Outlook

We have made a large advancement in understanding the use of ARP as an optical force, but work remains in order to understand it further. In this chapter I will lay out 3 possible avenues to probe the system further.

7.1 Interaction Time

One path forward would be to study the velocity dependence for significantly shorter interaction times. This would help to better understand the fidelity or repeatability of the inversion from each pulse pair.

Given a significantly shorter interaction time, one would safely presume a smaller deflection. By introducing additional beam pipe length, future experiments could clearly distinguish the magnitude of the force, allowing measurements of average force *vs.* number of pulse pairs, similar to Fig. 3.4.

7.2 Longitudinal Slowing

Prior to this thesis, it was thought that the values for Rabi frequency and chirp range that produced optimal forces for stationary atoms would also produce near optimal forces for moving atoms. The results shown in Fig. 6.6 lead us to believe that this view is wrong. Moving forward, it would be ideal to make velocity dependence measurements (like those pictured in Fig. 6.2) for an array of values for Rabi frequency and chirp range. Unfortunately, the current data collection process is far too lengthy for this to be reasonable.

As a possible solution, I propose that future experiments focus on longitudinal slowing of the atomic beam. This would require a large upgrade to the vacuum system, primary of which are a chopper for the atomic beam and determining the best solution for measuring the longitudinal velocity distribution.

While not giving the exact velocity dependence, one could ascertain some of the features of the velocity dependence by comparing the longitudinal velocity distribution with and without the ARP light. These measurements could be completed in a tiny fraction of the time currently dedicated to measurements. It would also allay some of the fears of equipment stability over experimental time scales.

A "forcemap-like" scan of optimal values for Rabi frequency and chirp range could be done with relative ease. The biggest challenge would actually be to parse through the large amount of data to probe the mysteries surrounding the evolution of forcemaps in Fig. 6.6.

Additionally, longitudinal slowing would provide the best test case scenario for characterizing the usefulness of the ARP force. This has been a long-term goal of the lab for well over a decade. This can help other experimenters to quantify whether the ARP force would be a useful technique to assist in their experiments.

7.3 Conventional ARP

A different path forward would be to consider changing the value of $\omega_m \approx 100\gamma$. As discussed in Sec. 3.3, our current experiments are operating in an unconventional parameter space. Ref. [33] suggests that the limit for the condition $\omega_m \gg \gamma$ is approximately $\omega_m > 20\gamma$. By lowering ω_m closer to this limit, we would have access to larger ratios of δ_0/ω_m and Ω_0/ω_m.

This would allow experiments to be conducted closer to the conventional parameter space for ARP. As seen in Fig. 3.6, this region is less sensitive to values for Rabi frequency and chirp range for stationary atoms. Measurements to determine if this remains true for moving atoms would be an important step in shedding some light on some of the mysteries raised in this thesis work.

Bibliography

[1] P. van der Straten and H. Metcalf. *Atoms and Molecules Interacting with Light*. Cambridge University Press, Cambridge, 2016.

[2] H. Metcalf and P. van der Straten. *Laser Cooling and Trapping*. Springer, New York, 1999.

[3] L. Allen and J.H. Eberly. *Optical Resonance and Two-Level Atoms*. Dover, New York, 1987.

[4] P. Meystre. *Atom Optics*. Springer-Verlag, New York, 2001.

[5] D. Budker, D.F. Kimball, and D.P. DeMille. *Atomic Physics: An Exploration through Problems and Solutions, 2nd Edition*. Oxford University Press, Oxford, 2008.

[6] P.R. Berman and V.S. Malinovsky. *Principles of Laser Spectroscopy and Quantom Optics*. Princeton University Press, Princeton, 2011.

[7] J.M. McGuirk, G.T. Foster, J.B. Fixler, M.J. Snadden, and M.A. Kasevich. Sensitive absolute-gravity gradiometry using atom interferometry. *Phys. Rev. A*, 65:033608, 2002.

[8] H. Walther, B.T.H. Varcoe, B.G. Englert, and T. Becker. Cavity quantum electrodynamics. *Reports on Progress in Physics*, 69:1352–1382, 2006.

[9] M.H. Anderson, J.R. Ensher, M.R. Matthews, C.E. Wieman, and E.A. Cornell. Observation of Bose-Einstein condensation in a dilute atomic vapor. *Science*, 269(5221): 198–201, 1995.

[10] K. Davis, M-O. Mewes, M. Andrews, M. van Druten, D. Durfee, D. Kurn, and W. Ketterle. Bose-Einstein condensation in a gas of sodium atoms. *Phys. Rev. Lett.*, 75:3969, 1995.

[11] C.C. Bradley, C.A. Sacket, and R.G. Hulet. Bose-Einstein condensation of lithium: Observation of limited condensate number. *Phys. Rev. Lett.*, 78:985, 1997.

[12] M. Greiner and S. Folling. Condensed-matter physics: Optical lattices. *Nature*, 453(7196):736–738, 2008.

[13] M. Lewenstein, A. Sanpera, V. Ahufinger, B. Damski, A.S. De, and U. Sen. Ultracold atomic gases in optical lattices: mimicking condensed matter physics and beyond. *Advances in Physics*, 56:243–379, 2007.

[14] M.R. Tarbutt. Laser cooling of molecules. *Contemporary Physics*, 59(4):356–376, 2018.

[15] E.S. Shuman, J.F. Barry, and D. DeMille. Laser cooling of a diatomic molecule. *Nature*, 467(7317):820–823, 2010.

[16] A. C. Vutha, W. C. Campbell, Y. V. Gurevich, N. R. Hutzler, M. Parsons, D. Patterson, E. Petrik, B Spaun, J. M. Doyle, G. Gabrielse, and D. DeMille. Search for the electric dipole moment of the electron with thorium monoxide. *Jour. of Phy. B: AMO Phy.*, 43 (7):074007, 2010.

[17] V. Zhelyazkova, A. Cournol, T.E. Wall, A. Matsushima, J.J. Hudson, E.A. Hinds, M.R. Tarbutt, and B.E. Sauer. Laser cooling and slowing of CaF molecules. *Phys. Rev. A*, 89:053416, 2014.

[18] B. Hemmerling, E. Chae, A. Ravi, L. Anderegg, G.K. Drayna, N.R. Hutzler, A.L. Collopy, J. Ye, W. Ketterle, and J.M. Doyle. Laser slowing of CaF molecules to near the capture velocity of a molecular MOT. *J. Phys. B*, 49:174001, 2016.

[19] S. Truppe, H.J. Williams, M. Hambach, L. Caldwell, N. J. Fitch, E.A. Hinds, B.E. Sauer, and M.R. Tarbutt. Molecules cooled below the Doppler limit. *Nature Physics*, 13:1173–1176, 2017.

[20] H.J. Williams, S. Truppe, M. Hambach, L. Caldwell, N.J. Fitch, E.A. Hinds, B.E. Sauer, and M.R. Tarbutt. Characteristics of a magneto-optical trap of molecules. *New Journal of Physics*, 19:113035, 2017.

[21] J.H.V. Nguyen, C.R. Viteri, E.G. Hohenstein, C.D. Sherrill, K.R. Brown, and B. Odom. Challenges of laser-cooling molecular ions. *New Journal of Physics*, 13, 2011.

[22] J.T. Bahns, W.C. Stwalley, and P.L. Gould. Laser cooling of molecules: A sequential scheme for rotation, translation, and vibration. *Journal of Chemical Physics*, 104(24): 9689–9697, 1996.

[23] W. Phillips and H. Metcalf. Laser deceleration of an atomic beam. *Phys. Rev. Lett.*, 48 (9):596–599, 1982.

[24] M.A. Weinstein. Thermodynamics of radiative emission processes. *Phys. Rev.*, 119:499, 1960.

[25] H.Metcalf. Colloquium: Strong optical forces on atoms in multifrequency light. *Reviews of Modern Physics*, 89:041001(18), 2017.

[26] H. Metcalf. Entropy exchange in laser cooling. *Physical Review A*, 77:061401, 2008.

[27] C. Corder, B. Arnold, and H. Metcalf. Laser cooling without spontaneous emission. *Physical Review Letters*, 114:043002, 2015.

[28] C. Corder, B. Arnold, X. Hua, and H. Metcalf. Laser cooling without spontaneous emission using the bichromatic force. *JOSA B*, 32(5):B75–B83, 2015.

[29] X. Hua, C. Corder, and H. Metcalf. Simulation of laser cooling by the bichromatic force. *Phys. Rev. A*, 93:063410, 2016.

[30] P.W. Milonni and J.H. Eberly. *Lasers*. Wiley, New York, 1988.

[31] C. Corder. *Optical Forces on Metastable Helium*. PhD thesis, Stony Brook University, 2014.

[32] Y. Wu and X. Yang. Strong-coupling theory of periodically driven two-level systems. *Phys. Rev. Lett.*, 98:013601, 2007.

[33] J. Elgin. *Study of the Velocity Dependence of the Adiabatic Rapid Passage (ARP) Optical Force in Helium*. PhD thesis, Stony Brook University, 2015.

[34] R. Feynman, F. Vernon, and R. Hellwarth. Geometrical representation of the Schrodinger equation for solving maser problems. *JOUAP*, 28(1):49–52, 1957.

[35] C. Gardiner and P. Zoller. *The Quantum World of Ultra-Cold Atoms and Light Book II: The Physics of Quantum-Optical Devices*. Imperial College Press, London, 2015.

[36] C. Cohen-Tannoudji, J. Dupont-Roc, and G. Grynberg. *Atom-Photon Interactions: Basic Processes and Applications*. John Wiley & Sons, New York, 1998.

[37] J. Bjorkholm, R. Freeman, A. Ashkin, and D. Pearson. Observation of focussing of neutral atoms by the dipole forces of resonance-radiation pressure. *Phys. Rev. Lett.*, 41 (20):1361, 1978.

[38] J. Söding, R. Grimm, Yu.B. Ovchinnikov, P. Bouyer, and C. Salomon. Short-distance atomic beam deceleration with a stimulated light force. *Phys. Rev. Lett.*, 78(8):1420–1423, 1997.

[39] V.S. Voitsekhovich, M.V. Danileiko, A.M. Negriiko, V.I. Romanenko, and L.P. Yatsenko. Light pressure on atoms in counterpropagating amplitude-modulated waves. *Zh. Tekh. Fiz.*, 58(6):1174–1176, 1988. [Sov. Phys. Tech. Phys. **33**, 690-691, (1988)].

[40] R. Grimm, J. Söding, and Yu.B. Ovchinnikov. Coherent beam splitter for atoms based on a bichromatic standing light-wave. *Optics Letters*, 19(9):658–660, 1994.

[41] L. Yatsenko and H. Metcalf. Dressed-atom description of the bichromatic force. *Phys. Rev. A*, 70(6):063402, 2004.

[42] C. Corder, B. Arnold, and H. Metcalf. Toward laser cooling without spontaneous emission, 2012. Poster presented at APS DAMOP.

[43] D. Stack. *Optical Forces from Periodic Adiabatic Rapid Passage Sequences on Metastable Helium Atoms*. PhD thesis, Stony Brook University, 2012.

[44] S.E. Galica, L. Aldridge, and E.E. Eyler. Four-color stimulated optical forces for atomic and molecular slowing. *Phys. Rev. A*, 88:043418, Oct 2013.

[45] N.V. Vitanov, T. Halfmann, B.W. Shore, and K. Bergmann. Laser-induced population transfer by adiabatic passage techniques. *Annual Review of Physical Chemistry*, 52: 763–809, 2001.

[46] M.A. Norcia, J.R.K. Cline, J.P. Bartolotta, M.J. Holland, and J.K. Thompson. Narrow-line laser cooling by adiabatic transfer. *New Journal of Physics*, 20, 2018.

[47] J. Bartolotta, M. Norcia, J. Cline, J. Thompson, and M. Holland. Laser cooling by sawtooth-wave adiabatic passage. *Phys. Rev. A*, 98:023404, 2018.

[48] V.S. Voitsekhovich, M.V. Danileiko, A.M. Negriiko, V.I. Romanenko, and L.P. Yatsenko. Observation of a stimulated radiation pressure of amplitude-modulated light on atoms. *Pisma Zhur. Teor. Eksp. Fiz.*, 49(3):138–140, 1989. [JETP Lett. 49, 161-164, (1989)].

[49] B. Nolle, H. Nolle, J. Schmand, and H.J. Andra. Atomic-beam deflection by double-pi-pulse laser technique. *Europhysics Letters*, 33(4):261–266, 1996.

[50] A. Goepfert, I. Bloch, D. Haubrich, F. Lison, R. Schutze, R. Wynands, and D. Meschede. Stimulated focusing and deflection of an atomic beam using picosecond laser pulses. *Phys. Rev. A*, 56(5):R3354–R3357, 1997.

[51] A. Abragam. *The Principles of Nuclear Magnetism*. Oxford Univ. Press, Oxford, 1961.

[52] E.B Treasy. Adiabatic inversion with light pulses. *Phys. Lett. A*, 27:421, 1968.

[53] M.M.T. Loy. Observation of population inversion by optical adiabatic rapid passage. *Phys. Rev. Lett.*, 32:814–817, 1974.

[54] C. Cohen-Tannoudji, J. Dupont-Roc, and G. Grynberg. *Atom-Photon Interactions*. J. Wiley & Sons, New York, 1992.

[55] J.C. Camparo and R.P. Frueholz. A dressed atom interpretation of adiabatic rapid passage. *J. Phys. B: At. Mol. Phys.*, 17(20):4169, 1984.

[56] E. Peik, M. Bendahan, I. Bouchoule, Y. Castin, and C. Salomon. Bloch oscillations of atoms, adiabatic rapid passage, and monokinetic atomic-beams. *Phys. Rev. A*, 55(4): 2989–3001, 1997.

[57] D. Stack, J. Elgin, P.M. Anisimov, and H. Metcalf. Numerical studies of optical forces from adiabatic rapid passage. *Phys. Rev. A*, 84:013420, 2011.

[58] X. Miao. *Optical Forces on Atoms with Periodic Adiabatic Rapid Passage Sequences*. PhD thesis, Stony Brook University, 2006.

[59] V.S. Malinovsky and J.L. Krausea. General theory of population transfer by adiabatic rapid passage with intense, chirped laser pulses. *Eur. Phys. J. D*, 14:147–155, 2001.

[60] C.P. Slichter. *Principles of Magnetic Resonance with Examples from Solid State Physics*. Harper & Row, New York, 1963.

[61] T. Lu, X. Miao, and H. Metcalf. Bloch theorem on the Bloch sphere. *Phys. Rev. A*, 71: 061405, 2005.

[62] S. S. Hodgman, R. G. Dall, L. J. Byron, K. G. H. Baldwin, S. J. Buckman, and A. G. Truscott. Metastable helium: A new determination of the longest atomic excited-state lifetime. *Phys. Rev. Lett.*, 103:053002, 2009.

[63] J. Kawanaka, M. Hagiuda, K. Shimizu, F. Shimizu, and H. Takuma. Generation of an intense low-velocity metastable-neon atomic beam. *Applied Physics B*, 56(1):21–24, 1993.

[64] H. Mastwijk. *Cold Collisions of Metastable Helium Atoms*. PhD thesis, Utrecht University, 1997.

[65] M. Cashen. *Optical Forces on Atoms in Polychromatic Light Fields*. PhD thesis, Stony Brook University, 2002.

[66] T. Inaki. Optical phase coherence in the adiabatic rapid passage force. Master's thesis, Stony Brook University, 2017.

[67] H. Zhang. Numerical study of adiabatic rapid passage sequences. Master's thesis, Stony Brook University, 2016.

[68] B.E.A. Saleh and M.C. Teich. *Fundamentals of Photonics*. John Wiley & Sons, New York, 1991.

[69] R.R. Alfano. *The Supercontinuum Laser Source*. Springer, New York, 2006.